The Lands cycle modulates plasma membrane lipid organization and insulin sensitivity in skeletal muscle

Patrick J. Ferrara,[1,2,5,9] Xin Rong,[3] J. Alan Maschek,[1,4] Anthony R.P. Verkerke,[1,2,5,9] Piyarat Siripoksup,[1,6] Haowei Song,[7] Karthickeyan C. Krishnan,[8] Jordan M. Johnson,[1,2,5,9] John Turk,[7] Joseph A. Houmard,[5,9] Aldons J. Lusis,[8] James E. Cox,[1,4,10] Saame Raza Shaikh,[5,11] Peter Tontonoz,[3] *Katsuhiko Funai[1,2,5,6,9,12,*]

[1]Diabetes and Metabolism Research Center, University of Utah, Salt Lake City, UT, USA
[2]Department of Nutrition and Integrative Physiology, University of Utah, Salt Lake City, UT, USA
[3]Department of Pathology and Laboratory Medicine, University of California, Los Angeles, Los Angeles, CA, USA
[4]Metabolomics, Mass Spectrometry, and Proteomics Core, University of Utah, Salt Lake City, UT, USA
[5]East Carolina Diabetes and Obesity Institute, East Carolina University, Greenville, NC, USA
[6]Department of Physical Therapy and Athletic Training, University of Utah, Salt Lake City, UT, USA
[7]Division of Endocrinology Metabolism and Lipid Research, School of Medicine, Washington University in St. Louis, St. Louis, MO, USA
[8]Department of Medicine, Cardiology Division at the University of California Los Angeles, Los Angeles, CA, USA
[9]Human Performance Laboratory, East Carolina University, Greenville, NC, USA
[10]Department of Biochemistry, University of Utah, Salt Lake City, UT, USA
[11]Department of Nutrition, University of North Carolina-Chapel Hill, Chapel Hill, NC, USA
[12]Molecular Medicine Program, University of Utah, Salt Lake City, UT, USA

*Correspondence:

Katsuhiko Funai, PhD

Diabetes & Metabolism Research Center

15 N, 2030 E, Salt Lake City, UT 84112

Phone: (801) 585-1781

Fax: (801) 585-0701

Email: kfunai@utah.edu

Conflict of Interest

The authors have declared that no conflict of interest exists.

Abstract

Aberrant lipid metabolism promotes the development of skeletal muscle insulin resistance, but the exact identity of lipid-mediated mechanisms relevant to human obesity remains unclear. A comprehensive lipidomic analyses of primary myocytes from lean insulin-sensitive (LN) and obese insulin-resistant (OB) individuals revealed several species of lysophospholipids (lyso-PL) that were differentially-abundant. These changes coincided with greater expression of lysophosphatidylcholine acyltransferase 3 (LPCAT3), an enzyme involved in phospholipid transacylation (Lands cycle). Strikingly, mice with skeletal muscle-specific knockout of LPCAT3 (LPCAT3-MKO) exhibited greater muscle lyso-PC/PC, concomitant with greater insulin sensitivity *in vivo* and insulin-stimulated skeletal muscle glucose uptake *ex vivo*. Absence of LPCAT3 reduced phospholipid packing of the cellular membranes and increased plasma membrane lipid clustering, suggesting that LPCAT3 affects insulin receptor phosphorylation by modulating plasma membrane lipid organization. In conclusion, obesity accelerates the skeletal muscle Lands cycle, whose consequence might induce the disruption of plasma membrane organization that suppresses muscle insulin action.

Introduction

Type 2 diabetes is the 7th leading cause of death in the United States (1) and is a major risk factor for cardiovascular disease, the leading cause of death (2). Skeletal muscle is the site of the largest glucose disposal in humans (3, 4). Insulin resistance in skeletal muscle is a necessary precursor to type 2 diabetes (5) and can be triggered by aberrant lipid metabolism (6-8). Several classes of lipids have been implicated in initiating cellular signals that suppress insulin action, but there has not been a clear consensus that these molecules are upregulated in skeletal muscle insulin resistance that occurs in the human population (9-14).

A difficulty in accurately measuring the muscle lipidome is confounded by the intramyofibrillar adipocytes which are particularly abundant in muscle biopsy samples from obese humans. Human skeletal muscle cells (HSkMC) are primary myoblasts that can be isolated, propagated, and differentiated from muscle biopsies. This *in vitro* system provides a unique model to study the skeletal muscle lipidome and signaling pathways free of contaminating cell types and circulating factors that affect muscle metabolism. Importantly, these HSkMC are known to retain their insulin sensitivity phenotype *ex vivo*, providing a platform to study mechanisms directly relevant to human physiology (15, 16).

In this study, we harvested HSkMC from lean insulin-sensitive (LN) and obese insulin-resistant (OB) subjects (Subject Characteristics: Table S1). We then propagated and differentiated these samples for analyses of the muscle lipidome, gene expression profile, insulin signaling, and membrane properties (Figure 1A). This approach led us to examine the lysophospholipid (lyso-PL) remodeling pathway (Lands cycle) as a potential diet-responsive mechanism that regulates skeletal muscle insulin action. Below we provide evidence that implicates this pathway in the pathogenesis of diet-induced skeletal muscle insulin resistance. Genetic or pharmacologic

suppression of this pathway was sufficient to enhance skeletal muscle insulin action *in vitro* and *in vivo*.

Results

A global lipidomic analysis of LN and OB myotubes revealed many classes of lipids that were differentially abundant (Figure 1B, Figure S1A-L). Among these, several species of lysophospholipids (lyso-PL), intermediates of the Lands cycle (17), were lower in OB HSkMC compared to LN (Figure 1C), a finding not previously described for an insulin-resistant state. While species of many classes of lyso-PL were reduced with obesity, the ratio of lyso-PL to its parent phospholipid were significantly lower for only lysophosphatidylcholine (lyso-PC)/phosphatidylcholine (PC) (Figure 1D). Previous studies suggest that altering the lyso-PC content of cell membranes is sufficient to alter the physical properties of membranes (18, 19). Consistent with this notion, phospholipid packing of LN and OB myotubes were remarkably different, with OB cells exhibiting more tightly packed membrane head groups compared to LN (Figure 1E&F). This occurred in the absence of changes in the phospholipid acyl-chain saturation index (Figure S1M).

What is the molecular mechanism by which obesity promotes a lower abundance of lyso-PL in skeletal muscle? LN and OB HSkMC utilized for the lipidomic analyses were cultured *ex vivo* for several weeks in identical media conditions. Thus, differences in the lipidome of these samples are likely the result of genetic and/or epigenetic influences, instead of hormonal or neuronal inputs that alter cells *in vivo*. We reasoned that such differential programming might be expected to manifest in gene expression profiles. A whole transcriptome sequencing of LN and OB myotubes revealed that lyso-PC acyltransferase 3 (LPCAT3), an enzyme of the Lands cycle, was more highly expressed with obesity. These findings were recapitulated in muscle biopsy samples (*not* myotubes) from LN and OB individuals as well as muscle tissue from wild-

type and db/db mice (Figure 1G). The Lands cycle represents a series of phospholipid-remodeling reactions by which acyl-chains become transacylated (17). Of the thirteen lyso-PL acyltransferase enzymes (20), LPCAT3 has the highest affinity for 16:0 and 18:0 lyso-PC, consistent with the specificity of reduced lyso-PC/PC (21, 22). Silencing of LPCAT3 in fibroblasts has been shown to increase Akt phosphorylation (23), while incubation of the same cells with 16:0/20:4 PC decreased Akt phosphorylation due to plasma-membrane specific effects (24). Mice with a liver-specific deletion of LPCAT3 exhibit enhanced ordering of membranes (25). In both human and mouse skeletal muscle, LPCAT3 is very highly expressed compared to other isoforms of LPCAT (Figure 1H), and skeletal muscle LPCAT3 expression is directly correlated to circulating insulin in 106 mouse strains (data not shown, bicor=0.296, P=0.0016) (26).

To study the role of LPCAT3 on skeletal muscle insulin action, we performed a lentivirus-mediated shRNA knockdown of LPCAT3 (Scrambled, SC; LPCAT3 knockdown, KD) in C2C12 myotubes (Figure 2A). LPCAT3 knockdown did not affect protein content for MyoD, various MHC isoforms, and respiratory complexes (Figure S2A-C), suggesting that the deletion of LPCAT3 has no effect on myotube lineage or mitochondrial density. Targeted lipidomic analyses revealed that LPCAT3 knockdown increased lyso-PC and decreased PC (Figure 2B&C), substrates and products of the LPCAT3-mediated reaction, respectively (27, 28). Together, these differences were sufficient to elevate lyso-PC/PC with LPCAT3 deletion (Figure 2D). Similar effects were seen with lipid species composed of an ethanolamine head group (Figure S2D-F), while the phospholipid saturation index increased with LPCAT3 knockdown (Figure S2G). Analogous to differences observed in LN and OB HSkMC, LPCAT3 deletion reduced phospholipid head group packing (Figure 2E&F). We then incubated SC and KD cells in a submaximal concentration of insulin to assess insulin signaling events. Strikingly, inhibition of LPCAT3 robustly enhanced insulin signaling with or without insulin (Figure 2G, Figure S2H).

Notably, the increase occurred at the level of the insulin receptor (IR), a node that is localized in the phospholipid-rich plasma membrane. Consequently, LPCAT3 deletion enhanced insulin-stimulated glycogen synthesis (Figure 2H), suggesting that this intervention increases skeletal muscle insulin sensitivity *in vitro* (due to low GLUT4:GLUT1 stoichiometry, insulin-stimulated glucose uptake is not an ideal surrogate for insulin sensitivity in C2C12 myotubes). LPCAT3 knockdown also enhanced insulin signaling in HSkMC from obese subjects (Figure 2G).

The organization and clustering of plasma membrane microdomains is linked to the induction of tyrosine-kinase signaling events, such as IR signaling (29-31). Because LPCAT3 deletion promoted enhanced insulin signaling at the level of IR phosphorylation, we visualized the organization of plasma membrane microdomains with labeling and patching of plasma membrane GM-1, a known marker of microdomains. Indeed, a greater proportion of C2C12 cells with LPCAT3 knockdown exhibited clustering of GM-1 enriched microdomains (Figure 2I, top &J). Furthermore, LPCAT3 deletion decreased the size of these clusters (Figure 2I, bottom &K), with no differences in total fluorescence from each cell (Figure S2I). These data indicate that LPCAT3 inhibition induces a reorganization of plasma membrane microdomains, potentially explaining increased IR phosphorylation.

Next, we examined whether inhibition of muscle LPCAT3 would promote greater insulin sensitivity *in vivo*. Mice with tamoxifen-inducible skeletal muscle-specific knock-out of LPCAT3 (LPCAT3-MKO) were generated by crossing the HSA-MerCreMer mice (34) with LPCAT3 conditional knock-out mice (exon3 of the *Lpcat3* gene flanked with *loxP* sites) (25) (Figure 3A). This strategy successfully yielded mice with suppressed LPCAT3 expression in skeletal muscle without affecting other tissues (Figure 3B), and without compensatory upregulation of other members of the LPCAT family (Figure 3C). Control and LPCAT3-MKO mice gained weight equally when fed a high-fat diet (HFD, Figure 3D) with no difference in adipose tissue weight at

the end of diet intervention (Figure 3E). Food consumption, whole-body oxygen consumption, spontaneous activity, and respiratory exchange ratio were similarly not different between groups (Figure 3F-I). Fasting glucose, insulin, and glucose tolerance (Figure 3J-L) were unchanged, but circulating insulin during the glucose tolerance test was substantially lower in LPCAT3-MKO mice compared to the control group (Figure 3M).

To evaluate whether improved glycemic efficiency was attributable to greater skeletal muscle insulin sensitivity, we quantified insulin-stimulated skeletal muscle glucose uptake *ex vivo*. Isolated muscles from HFD-fed control and LPCAT3-MKO mice were incubated with or without a submaximal concentration of insulin for the measurement of 2-deoxy-glucose uptake. Indeed, insulin-stimulated skeletal muscle glucose uptake was robustly enhanced in LPCAT3-MKO mice compared to control (Figure 4A). The increase in glucose uptake coincided with augmented insulin-stimulated Akt phosphorylation (Figure 4B&C), similar to C2C12 and human primary myotubes (Figure 2). These results suggest that inhibition of muscle LPCAT3 increases skeletal muscle insulin sensitivity *in vivo*. Similar to results from LPCAT3 knockdown *in vitro*, muscles from LPCAT3-MKO mice had elevated lyso-PC (16:0 and 18:0) (Figure 4D) and lower levels of PC species known to be the main products of the LPCAT3 reaction (16:0/18:2 and 16:0/22:4) (Figure 4E) (22, 35, 36). As a result, lyso-PC/PC was ~2-fold greater in LPCAT3-MKO mice compared to control (Figure 4F). In contrast, lyso-PE/PE or phospholipid saturation index was unaltered between control and LPCAT3-MKO muscles (Figure S3A-D), similar to the lipidome in LN and OB HSkMC (Figure 1&S1). Muscles from control and LPCAT3-MKO did not differ in mass, length, force-generating capacity, fiber-type distribution, or content of proteins in the electron transport chain (Figure 4G-L, Figure S3E-G).

How does the inhibition of the Lands cycle promote greater insulin action in skeletal muscle? LPCAT3 deficiency enhanced insulin signaling at the level of IR which was concomitant with

183 altered plasma membrane lipid organization (Figure 2), suggesting that changes in plasma
184 membrane properties may mediate the insulin-sensitizing effects. Membrane organization is
185 vital to insulin action, as IR is localized to highly ordered microdomains on the plasma
186 membrane (37, 38). The interaction between caveolae and IR enhances insulin signaling in
187 other cell types (39, 40). Mice that lack caveolin-3 (cav3), a skeletal muscle-specific scaffolding
188 protein critical in the formation of caveolae on the plasma membrane, exhibit skeletal muscle
189 insulin resistance due to plasma membrane-specific effects on the IR (41, 42). Overexpression
190 of dominant-negative cav3 leads to decreased glucose uptake and glycogen synthesis in
191 C2C12 cells, which is attributed to decreased Akt phosphorylation (43-45). Conversely, an
192 increase in wildtype cav3 expression is sufficient to enhance Akt phosphorylation and glucose
193 uptake (46). Indeed, LPCAT3 knockdown substantially increased cav3 content in C2C12
194 myotubes (Figure 5A). To examine the possibility that the absence of LPCAT3 increases the
195 abundance of lipids in caveolae, we isolated membrane fractions from C2C12 myotubes with or
196 without LPCAT3 deletion and subjected them for further purification by density-gradient
197 ultracentrifugation.
198
199 Cholesterol and sphingomyelin are two classes of lipids that are more highly abundant in the
200 detergent-resistant membrane (DRM; i.e. ordered membrane) fraction compared to the
201 detergent-soluble membrane (DSM) fraction (47). Experiments in wild-type C2C12 myotubes
202 indicated that fractions 4-5 have substantial amounts of total lipid (Figure S5A). These fractions
203 were enriched in sphingomyelin and cholesterol which are known to be conducive for more
204 highly ordered membrane (Figure S5B&C), with relatively low abundance of lipids involved in
205 the LPCAT3-mediated reaction (Figure S5D-G). LPCAT3 knockdown did not appear to alter the
206 overall content of lipid in the DRM fraction, nor did it affect enrichment of sphingomyelin and
207 cholesterol (Figure 5B&C). Even though the DRM fraction is known to contain very little protein
208 (48), we detected substantial cav3 in both SC and KD myotubes (Figure 5D). While LPCAT3

deletion did not affect the proportion of cav3 in the DRM fraction, it is noteworthy that elevated cav3 content with LPCAT3 knockdown (Figure 5A) is reflected in the DRM fraction. This is particularly interesting considering there was no enrichment of sphingomyelin or cholesterol in the DRM fraction, which may have been expected given that these lipids induce sequestration of cav3 into caveolae. Consistent with this notion, LPCAT3 deletion was sufficient to elevate lyso-PC in the DRM as well as DRM fractions of the membrane (Figure 5E), with minimal effect on PC species (Figure S5A). Similar results were exhibited with lyso-PE and PE (Figure S5B&C). The saturation index of phospholipids was slightly increased in both DRM and DSM fractions, which may also contribute to the increase in the plasma membrane lipid clustering (Figure S5D). Thus, LPCAT3 deletion promotes the accumulation of lyso-PC in the DRM fraction which may contribute to membrane organization. To test our hypothesis that an increase in membrane organization mediates the insulin-sensitizing effect of LPCAT3 deletion, we incubated C2C12 myotubes with methyl-beta-cyclodextrin (MβCD), a cholesterol-depleting compound that disrupts plasma membrane microdomains (49). Indeed, incubation of cells with MβCD decreased cav3 protein content (Figure 5F) without decreasing the abundance of flotillin-1 (Figure 5G), a protein associated with non-caveolar microdomains. MβCD treatment normalized insulin-stimulated Akt phosphorylation with LPCAT3 deletion to control levels (Figure 5H). These findings are consistent with the notion that LPCAT3 deletion enhances IR signaling by its effect on plasma membrane organization.

CI-976 is a pan lysophospholipid acyltransferase inhibitor (32, 33) that has the ability to disrupt Lands cycle, similar to LPCAT3 deletion. To examine a possibility that the insulin-sensitizing effect of LPCAT3 knockdown is attributable to an unknown function of LPCAT3 outside of the Lands cycle, we studied C2C12 myotubes with or without CI-976. Consistent with our findings with LPCAT3 knockdown (Figure 2E&F), pre-incubation of wild-type C2C12 myotubes with CI-976 robustly decreased phospholipid headgroup packing (Figure 5I). Strikingly, CI-976 also

promoted an increase in insulin-stimulated Akt phosphorylation compared to vehicle control (Figure 5J). These evidence support our findings that inhibition of Lands cycle alter plasma membrane property to increase skeletal muscle insulin sensitivity.

Discussion

Obesity promotes aberrant lipid metabolism in various tissues including skeletal muscle where it dampens its ability to respond to circulating insulin and increase glucose uptake. Studies in model organisms have led to the identification of lipotoxic lipids that might promote insulin resistance in various tissues (50, 51), but some studies were unable to validate these mechanisms in human muscles (52, 53). To gain a global understanding of changes that occur in muscle lipid metabolism with human obesity, we conducted lipidomic analyses on muscle samples from LN and OB subjects. Obesity was associated with decreases in various species of lysophospholipids, an observation that had never been previously reported. Many of these lipids are generated by the enzymes of the Lands cycle, which removes fatty-acyl chains at the sn-2 position of phospholipids to generate lysophospholipids (Lands cycle). We propose a novel mechanism by which obesity accelerates the skeletal muscle Lands cycle to promote insulin resistance.

The acceleration of muscle phospholipid transacylation was apparently driven by increased LPCAT3 expression, likely attributable to diet-induced activation of LXRs and PPARs (22, 54, 55). The inhibition of LPCAT3 enhances insulin signaling at the level of IR to improve skeletal muscle insulin sensitivity. We believe that the insulin-sensitizing effect of Lands cycle inhibition is mediated by its effect on the plasma membrane lipid organization (Figure 6). Consistent with this notion, LPCAT3 deletion and/or CI-976 treatment was sufficient to alter membrane phospholipid packing, GM1-microdomain clustering, cav3 content and lipid composition of detergent-resistant and –soluble membranes. Furthermore, disruption of cholesterol-rich

microdomains was sufficient to eliminate the insulin-sensitizing effect of LPCAT3 inhibition. Interventions that interfere with the plasma membrane organization would be predicted to have effects on other cellular events, but the deletion of LPCAT3 did not appear to have an overly adverse effect on skeletal muscle, including mass, fiber-type or force-generating capacity. It would be of substantial interest to pursue implications of altered Lands cycle and/or plasma membrane organization in the context of other cellular events including signaling through other receptor tyrosine kinases.

Observations in this study open up a potential opportunity to pharmacologically target this pathway (such as with CI-976) to enhance skeletal muscle insulin sensitivity and improve whole-body glucose homeostasis. It is noteworthy that the current study partly drew its conclusions from lipidomic analyses and loss-of-function studies performed in human samples, suggesting that this mechanism may be directly involved in the pathogenesis of skeletal muscle insulin resistance in human obesity. We are also interested in examining whether obesity induces similar changes in plasma membrane organization of other tissues to promote pathology.

Methods

Human Subjects

All participants were prescreened to be free of any known metabolic diseases or heart conditions, nontobacco users, not taking any medications known to alter metabolism, and sedentary. Six lean subjects without diabetes (LN: BMI < 25 kg/m^2) and six subjects with severe obesity (OB: BMI > 40 kg/m^2) were studied (all Caucasian females). The subjects were instructed not to exercise for approximately 48h before the muscle biopsy. A fasting blood sample (glucose and insulin) and muscle biopsy from the vastus lateralis were collected. A portion of the biopsy sample was frozen immediately, and another portion was used to isolate primary muscle cells.

Cell Culture

Primary human skeletal muscle cells (HSkMC) were isolated from fresh muscle biopsies as previously described (15, 56). HSkMC were cultured in growth media containing low glucose DMEM, 10x FBS, 0.5 mg/mL BSA, 0.5 mg/mL fetuin, 10 ng/mL human EGF, 1 µM dexamethasone, and 0.1% penicillin-streptomycin. HSkMC were differentiated in low glucose DMEM, 2% horse serum, 0.5 mg/mL BSA, 0.5 mg/mL fetuin, and 0.1% penicillin-streptomycin. C2C12 myoblasts were grown in high glucose DMEM (4.5 g/L glucose, [+]L-Glutamine; Gibco 11965-092) supplemented with 10% FBS (Heat Inactivated, Certified, US Origin; Gibco 10082-147), and 0.1% penicillin-streptomycin (10,000 U/mL; Gibco 15140122). C2C12 cells were differentiated into myotubes with low glucose DMEM (1 g/L glucose, [+]L-Glutamine, [+]110 mg/L sodium pyruvate; Gibco 11885-084) supplemented with 2% horse serum (Defined; VWR 16777), and 0.1% penicillin-streptomycin. For experiments with CI-976 C2C12 myoblasts were differentiated with either 10 µM of CI-976 or equal volume DMSO (vehicle). For experiments with methyl-beta-cyclodextrin cells were incubated with 10 mM (1320 g/mole) for 1 hour directly

dissolved into media. Prior to all experiments cells were serum-starved for 3 hours in low glucose DMEM containing 1% BSA and 0.1% penicillin-streptomycin.

Quantitative-RT-PCR

Samples were homogenized in TRIzol reagent (Life Technologies, Grand Island, NY) to extract total RNA. 1 µg RNA was reverse transcribed using IScript™ cDNA synthesis kit (Biorad, Hercules, CA). RT-PCR was performed with the Viia™ 7 Real-Time PCR System (Life Technologies, Grand Island, NY) using SYBR® Green reagent (Life Technologies, Grand Island, NY). All data were normalized to ribosomal L32 gene expression and primer sequences are provided (Extended Data Table 2).

Mass Spectrometry

Global lipidomic analyses for LN and OB HSkMC were performed at the Mass Spectrometry Resource at the Washington University School of Medicine (15). Extracted lipids with internal standards were analyzed with a Thermo Vantage triple-quadrupole mass spectrometer or a Thermo Trace GC Ultra mass spectrometer. Targeted lipidomic analyses for C2C12 myotubes and mouse skeletal muscles were conducted in the Metabolomics Core at the University of Utah (57-59). Extracted lipids with internal standards were analyzed with an Agilent triple-quadrupole mass spectrometer. The quantity of each lipid species was normalized to total lipid content for DRM/DSM experiments or to the total protein content for all others. The phospholipid saturation index was quantified by multiplying the relative abundance of each phospholipid species by the total number of double bonds in the acyl chains of that species.

Merocyanine 540

Merocyanine 540 (MC540) measurements were taken as previously described (60). In short, skeletal muscle cells (C2C12 and HSkMC) were fully differentiated and 2 million were used for

measurements. Cells were washed with Hanks Balanced Salt Solution (HBSS; Gibco 14025092) prior to re-suspension in a cuvette with HBSS. MC540 in DMSO was added at a final concentration of 0.2 µM and after a 10-minute dark incubation, an emission scan was performed ranging from 550-750 nm with fluorescence excitation set at 540 nm on a PTI QuantaMaster 6000 Fluorimeter.

Lentivirus-Mediated Knockdown of LPCAT3

LPCAT3 expression was decreased using pLKO.1 lentiviral-RNAi system. Plasmids encoding shRNA for mouse LPCAT3 (shLPCAT3: TRCN0000121437) were obtained from Sigma (St. Louis, MO). Packaging vector psPAX2 (ID #12260), envelope vector pMD2.G (ID #12259) and scrambled shRNA plasmid (sc: ID1864) were obtained from Addgene (Cambridge, MA). HEK293T cells in 10 cm dishes were transfected using 50µL 0.1% Polyethylenimine, 200µL 0.15 M Sodium Chloride, and 500 µL Opti-MEM ([+] Hepes, [+] 2.4 g/L Sodium Bicarbonate, [+] L-Glutamine; Gibco 31985) with 2.66 µg of psPAX2, 0.75 µg of pMD2.G, and 3 µg of either scrambled or LPCAT3 shRNA plasmid. After 48 hours, growth media was collected, filtered using 0.22 µm vacuum filters, and used to treat undifferentiated HSkMC or C2C12 cells for 48 hours. To ensure only cells infected with shRNA vectors were viable, cells were selected with puromycin throughout differentiation.

Western Blot

Whole muscle or cells were homogenized and Western blots were performed as previously described (56). Protein homogenates were analyzed for abundance of phosphorylated(Tyr972)-insulin receptor (Invitrogen: 44-800G), insulin receptor-β (Cell Signaling: 3020S), phosphorylated(Thr308)-Akt (Cell Signaling: 9275S), phosphorylated(Ser472)-Akt (Cell Signaling: 9271L), Akt (Cell Signaling: 9272S), phosphorylated(Thr642)-AS160 (Cell Signaling: 8881), AS160 (Millipore Sigma: 07-741), MyoD (DSHB: D7F2), mitochondrial complexes I-V

(Abcam: ab110413), MHC type I (DSHB: A4.840), MHC type IIa (DSHB: SC-71), MHC type IIx (DSHB: 6H1), MHC type IIb (DSHB: BF-F3), MHC neo (DSHB: N1.551), MHC emb (DSHB: BF-G6), Caveolin-3 (BD Biosciences: 610-420), Na/K ATPase (Cell Signaling: 3010S), Flotillin-1 (Cell Signaling: 3253), and actin (Millipore Sigma: A2066).

Glycogen Synthesis

The glycogen synthesis rate was quantified as previously described (61, 62). Briefly, cells were incubated in media containing D-[U-^{14}C] glucose with (12 nM) or without insulin for 2h at 37 °C. Cells were then washed with ice-cold PBS and homogenized for 1h with 0.05% SDS. Part of the lysate was used for a protein assay and the other was combined with 2mg carrier glycogen and incubated at 100 °C for 1h. Ice cold ethanol (100%) was added to the boiled samples prior to overnight rocking at 4 °C. Samples were then centrifuged at 11,000 xG for 15 min at 4 °C to pellet glycogen. Pellets were re-suspended in de-ionized H_2O and glycogen synthesis was calculated with liquid scintillation.

Generation of LPCAT3 Skeletal Muscle-Specific Knock Out Mice

Conditional LPCAT3 knock out (LPCAT3cKO+/+) mice were previously generated by flanking exon3 of the *Lpcat3* gene with *loxP* sites (25). LPCAT3cKO+/+ mice were then crossed with tamoxifen-inducible, skeletal muscle-specific Cre-recombinase (HSA-MerCreMer+/-)(34) mice to generate LPCAT3cKO+/+;HSA-MerCreMer-/- (Control; Ctrl) and LPCAT3cKO+/+;HSA-MerCreMer+/- (LPCAT3 Muscle-specific Knock-Out; LPCAT3-MKO). Tamoxifen injected (7.5 µg/g body mass, 5 consecutive days) control and LPCAT3-MKO littermates were used for all experiments. Mice were maintained on a 12 h light/dark cycle in a temperature-controlled room. Prior to all terminal experiments and tissue harvesting, mice were given an intraperitoneal injection of 80 mg/kg ketamine and 10 mg/kg xylazine.

Glucose Tolerance Test

Intra-peritoneal glucose tolerance tests were performed by injecting 1 mg glucose/g body mass. Mice were fasted for 4 hours prior to glucose injection. Blood glucose was measured prior to glucose injection and 15, 30, 60, and 120 minutes post-injection via tail bleed with a handheld glucometer (Bayer Contour 7151H). In a separate set of experiments, mice were injected with 1 mg glucose/g body mass and blood was taken from the facial vein at the 30-minute time point for insulin quantification.

Serum Insulin and Glucose Quantification

Blood was collected from the facial vein either prior to anesthesia or at the 30-minute time point of the glucose tolerance test. Blood was then placed at room temperature for 20 minutes to allow for clotting before centrifugation at 2,000 xG for 10 minutes at 4°C. The supernatant (serum) was placed in a separate tube and stored at -80 °C until analysis.

Serum glucose was quantified using a colorimetric assay. A glucose standard curve was generated (Millipore Sigma, G6918) and serum samples were mixed with a PGO enzyme (Millipore Sigma, P7119) and colorimetric substrate (Millipore Sigma, F5803) and measured at OD450 on a plate reader. Serum insulin was quantified using an insulin mouse serum kit (CisBio, 62IN3PEF) using Fluorescence Resonance Energy Transfer on a plate reader (ThermoFisher, Varioskan LUX).

[^{3}H]2-Deoxy-D-Glucose Uptake

Ex vivo glucose uptake was measured in the soleus muscle as previously described (63, 64). In brief, soleus muscles were dissected and placed in a recovery buffer (KHB with 0.1% BSA, 8 mM glucose, and 2 mM mannitol) at 37 °C for 10 minutes. After incubation in recovery buffer, muscles were moved to pre-incubation buffer (KHB with 0.1% BSA, 2 mM sodium pyruvate, and 6 mM mannitol) ± 200 µU/mL insulin for 15 minutes. After pre-incubation muscles were placed

in incubation buffer (KHB with 0.1% BSA, 9 mM [^{14}C]mannitol, 1 mM [^{3}H]2-deoxyglucose) ± 200 µU/mL insulin for 15 minutes. Contralateral muscles were used for basal or insulin-stimulated measurements. After incubation muscles were blotted dry on ice-cold filter paper, snap-frozen, and stored at -80 °C until analyzed with liquid scintillation counting.

Muscle Force Generation

Force generating properties of extensor digitorum longus (EDL) muscles were measured as previously described (65). Briefly, EDL muscles were sutured at each tendon and muscles were suspended at optimal length (L_o) which was determined by pulse stimulation. After L_o was identified muscles were stimulated (0.35 s, pulse width 0.2 ms) at frequencies ranging from 10-200 Hz. Muscle length and mass were measured to quantify CSA (66-68) for force normalization.

Muscle Immunohistochemistry

Frozen, OCT-embedded hind limb muscle samples (tibialis anterior or EDL) were sectioned at 10µm using a cryostat (Microtome Plus™). Following 1h blocking with M.O.M mouse IgG blocking (Vector: MKB-2213), myofiber sections were incubated for 1h with concentrated BA.D5, SC.71, and BF.F3 (all 1:100; DSHB) and laminin (1:200; Millipore Sigma: L9393) in 2.5% normal horse serum. To visualize laminin (for fiber border), myosin heavy chain I (MHC I), myosin heavy chain IIa (MHC IIa), and myosin heavy chain IIb (MHC IIb), slides were incubated for 1h with the following secondaries: AMCA (1:250 Vector: CI-1000), Alexa Fluor 647 (1:250; Invitrogen: A21242), Alexa Fluor 488 (1:500; Invitrogen: A21121) and Alexa Fluor 555 (1:500; Invitrogen: A21426), respectively. Negatively stained fibers were considered myosin heavy chain IIx (MHC IIx). After staining, slides were coverslipped with mounting media (Vector: H-1000). Stained slides were imaged with a fully automated wide-field light microscope (Nikon,

Nikon Corp.; Tokyo, Japan) with a 10X objective lens. Images were captured using high sensitivity Andor Clara CCD (Belfast, UK).

GM-1 Labeling and Imaging

GM-1 clusters were labeled using a Vybrant® Alexa Fluor® 488 Lipid Raft Labeling Kit (ThermoFisher Scientific: V34404) as previously described (69). Briefly, 2 million myotubes were incubated 1mL in ice-cold starvation media with 0.8µg/mL fluorescent cholera toxin subunit B conjugate (CT-B) for 10 minutes. CT-B conjugates were then cross-linked with an anti-CT-B antibody (1:200) in ice-cold starvation media for 15 minutes. Cells were fixed for 1 h at 4 ˚C in ice-cold 4% paraformaldehyde in PBS in dark. Between each step, cells were washed 2x in ice-cold PBS. Cells were imaged on an Olympus FV1000 confocal microscope (2.5x, HV:600, offset: 30). Images were processed using NIH ImageJ. All images were background subtracted with a rolling ball radius of 50 pixels. Images were blindly scored by S.R.S and K.F. as exhibiting clustering of microdomains or non-clustering. Images were then subjected to color thresholding using the Otsu method (70, 71) (designed for thresholding images for cluster analyses) and made binary. A particle analysis of all particles that were >0.1µm^2 was performed to determine the average cluster size for each cell that was imaged (72). For each experiment, 35-50 cells per group were analyzed and the median was taken as a representative of that experiment.

Detergent-Resistant Membrane Isolation

Detergent-resistant membranes (DRM) and detergent-soluble membranes (DSM) were isolated as previously described (72). Briefly, 2x15 cm plates of cells were scraped in ice-cold PBS and then pelleted. Cells were re-suspended in 1mL of cold homogenization buffer (Mes-buffered saline [MBS], 1% Triton-X wt/v, and protease and phosphatase inhibitor) and passed through a 23-gauge needle 6 times before incubating at 4 °C for 30 minutes. MBS was added to the homogenate until a volume of 2.5 mL was reached then mixed with 2.5 mL of 90% sucrose in

MBS and 4mL of this mixture was added to an ultracentrifuge tube (Beckman Coulter 344061). A sucrose gradient was generated by adding 4 mL 35% sucrose followed by 4mL of 5% sucrose. Samples were then centrifuged at 100,000 xG at 4 °C for 20 hours in a swinging bucket rotor (Beckman L8-M Ultracentrifuge, SW28 Rotor).

Statistics

Statistical analysis was performed using Prism 7 software (GraphPad). Student's t-tests were performed with data composed of 2 groups and 2-way ANOVA for multiple groups followed by Sidak's multiple comparison test. All data are Mean±SEM and statistical significance was set at $P<0.05$.

Study Approval

The experimental protocol was approved by the Internal Review Board for Human Research at East Carolina University. Informed consent was obtained prior to inclusion in the study.

Animal experiments were approved by the University of Utah Institutional Animal Care and Use Committee.

Author contributions

P.J.F. and K.F. contributed to study concept design and wrote the manuscript. J.A.H. performed human muscle biopsies. J.M.J. contributed to study concept and design and data analysis. X.R. and P.T. developed LPCAT3 conditional knock-out mice. J.A.M., J.E.C., H.S., and J.T. performed mass spectrometry analyses. P.J.F., K.F., and S.R.S. performed analyses of the physical properties of phospholipid membranes. A.R.P.V. and P.J.F. performed analysis of muscle force production. P.S. performed muscle histology measurements. P.J.F. performed all biochemical assays and metabolic phenotyping measurements. K.C.K. and A.J.L. performed

483 correlation analyses with 106 mouse strains. J.A.H., P.T., J.T., J.E.C., and S.R.S. edited the
484 manuscript.
485
486 **Acknowledgments**
487 This work was supported by NIH grants DK107397, DK109888, AG063077 (to K.F.), HL030568,
488 HL030568, HL136618 (to P.T.), AT006122, HL123647 (to S.R.S.), HL028481, HL030568 (to
489 A.J.L.), and DK056112 (to J.A.H.), American Heart Association 18PRE33960491 (to A.R.P.V.),
490 American Heart Association 19PRE34380991 (to J.M.J.), and the Larry H. and Gail Miller
491 Family Foundation (to P.J.F). The University of Utah Metabolomics, Mass Spectrometry, and
492 Proteomics core is supported by S10 OD016232, S10 OD021505, and U54 DK110858. The
493 Washington University Biomedical MS Resource is supported by United States Public Health
494 Services grants P41-GM103422, P30-DK020579, and P30-DK056341.

References

1. Heron M. Deaths: Leading Causes for 2017. *National Vital Statistics Reports.* 2019;68(6).
2. Huo X, Gao L, Guo L, Xu W, Wang W, Zhi X, Li L, Ren Y, Qi X, Sun Z, et al. Risk of non-fatal cardiovascular diseases in early-onset versus late-onset type 2 diabetes in China: a cross-sectional study. *Lancet Diabetes Endocrinol.* 2016;4(2):115-24.
3. DeFronzo RA, Jacot E, Jequier E, Maeder E, Wahren J, and Felber JP. The effect of insulin on the disposal of intravenous glucose. Results from indirect calorimetry and hepatic and femoral venous catheterization. *Diabetes.* 1981;30(12):1000-7.
4. Thiebaud D, Jacot E, DeFronzo RA, Maeder E, Jequier E, and Felber JP. The effect of graded doses of insulin on total glucose uptake, glucose oxidation, and glucose storage in man. *Diabetes.* 1982;31(11):957-63.
5. DeFronzo RA, and Tripathy D. Skeletal muscle insulin resistance is the primary defect in type 2 diabetes. *Diabetes Care.* 2009;32 Suppl 2(S157-63.
6. Dube JJ, Coen PM, DiStefano G, Chacon AC, Helbling NL, Desimone ME, Stafanovic-Racic M, Hames KC, Despines AA, Toledo FG, et al. Effects of acute lipid overload on skeletal muscle insulin resistance, metabolic flexibility, and mitochondrial performance. *Am J Physiol Endocrinol Metab.* 2014;307(12):E1117-24.
7. Manco M, Mingrone G, Greco AV, Capristo E, Gniuli D, De Gaetano A, and Gasbarrini G. Insulin resistance directly correlates with increased saturated fatty acids in skeletal muscle triglycerides. *Metabolism.* 2000;49(2):220-4.
8. Lee JS, Pinnamaneni SK, Eo SJ, Cho IH, Pyo JH, Kim CK, Sinclair AJ, Febbraio MA, and Watt MJ. Saturated, but not n-6 polyunsaturated, fatty acids induce insulin resistance: role of intramuscular accumulation of lipid metabolites. *J Appl Physiol (1985).* 2006;100(5):1467-74.
9. Chavez JA, and Summers SA. Characterizing the effects of saturated fatty acids on insulin signaling and ceramide and diacylglycerol accumulation in 3T3-L1 adipocytes and C2C12 myotubes. *Arch Biochem Biophys.* 2003;419(2):101-9.
10. Bergman BC, Hunerdosse DM, Kerege A, Playdon MC, and Perreault L. Localisation and composition of skeletal muscle diacylglycerol predicts insulin resistance in humans. *Diabetologia.* 2012;55(4):1140-50.
11. Perreault L, Newsom SA, Strauss A, Kerege A, Kahn DE, Harrison KA, Snell-Bergeon JK, Nemkov T, D'Alessandro A, Jackman MR, et al. Intracellular localization of diacylglycerols and sphingolipids influences insulin sensitivity and mitochondrial function in human skeletal muscle. *JCI Insight.* 2018;3(3).
12. Adams JM, 2nd, Pratipanawatr T, Berria R, Wang E, DeFronzo RA, Sullards MC, and Mandarino LJ. Ceramide content is increased in skeletal muscle from obese insulin-resistant humans. *Diabetes.* 2004;53(1):25-31.
13. Schmitz-Peiffer C, Craig DL, and Biden TJ. Ceramide generation is sufficient to account for the inhibition of the insulin-stimulated PKB pathway in C2C12 skeletal muscle cells pretreated with palmitate. *J Biol Chem.* 1999;274(34):24202-10.
14. Itani SI, Ruderman NB, Schmieder F, and Boden G. Lipid-induced insulin resistance in human muscle is associated with changes in diacylglycerol, protein kinase C, and IkappaB-alpha. *Diabetes.* 2002;51(7):2005-11.
15. Paran CW, Verkerke AR, Heden TD, Park S, Zou K, Lawson HA, Song H, Turk J, Houmard JA, and Funai K. Reduced efficiency of sarcolipin-dependent respiration in myocytes from humans with severe obesity. *Obesity (Silver Spring).* 2015;23(7):1440-9.
16. Hulver MW, Berggren JR, Carper MJ, Miyazaki M, Ntambi JM, Hoffman EP, Thyfault JP, Stevens R, Dohm GL, Houmard JA, et al. Elevated stearoyl-CoA desaturase-1

expression in skeletal muscle contributes to abnormal fatty acid partitioning in obese humans. *Cell Metab.* 2005;2(4):251-61.

17. Lands WE. Metabolism of glycerolipides; a comparison of lecithin and triglyceride synthesis. *J Biol Chem.* 1958;231(2):883-8.
18. Fink KL, and Gross RW. Modulation of canine myocardial sarcolemmal membrane fluidity by amphiphilic compounds. *Circ Res.* 1984;55(5):585-94.
19. Bing RJ, Termin A, Conforto A, Dudek R, and Hoffmann MJ. Membrane function and vascular reactivity. *Biosci Rep.* 1993;13(2):61-7.
20. Hishikawa D, Hashidate T, Shimizu T, and Shindou H. Diversity and function of membrane glycerophospholipids generated by the remodeling pathway in mammalian cells. *J Lipid Res.* 2014;55(5):799-807.
21. Kazachkov M, Chen Q, Wang L, and Zou J. Substrate preferences of a lysophosphatidylcholine acyltransferase highlight its role in phospholipid remodeling. *Lipids.* 2008;43(10):895-902.
22. Zhao Y, Chen YQ, Bonacci TM, Bredt DS, Li S, Bensch WR, Moller DE, Kowala M, Konrad RJ, and Cao G. Identification and characterization of a major liver lysophosphatidylcholine acyltransferase. *J Biol Chem.* 2008;283(13):8258-65.
23. Pein H, Koeberle SC, Voelkel M, Schneider F, Rossi A, Thurmer M, Loeser K, Sautebin L, Morrison H, Werz O, et al. Vitamin A regulates Akt signaling through the phospholipid fatty acid composition. *FASEB J.* 2017;31(10):4566-77.
24. Koeberle A, Shindou H, Koeberle SC, Laufer SA, Shimizu T, and Werz O. Arachidonoyl-phosphatidylcholine oscillates during the cell cycle and counteracts proliferation by suppressing Akt membrane binding. *Proc Natl Acad Sci U S A.* 2013;110(7):2546-51.
25. Rong X, Wang B, Dunham MM, Hedde PN, Wong JS, Gratton E, Young SG, Ford DA, and Tontonoz P. Lpcat3-dependent production of arachidonoyl phospholipids is a key determinant of triglyceride secretion. *Elife.* 2015;4(
26. Parks BW, Sallam T, Mehrabian M, Psychogios N, Hui ST, Norheim F, Castellani LW, Rau CD, Pan C, Phun J, et al. Genetic architecture of insulin resistance in the mouse. *Cell Metab.* 2015;21(2):334-47.
27. Eto M, Shindou H, Koeberle A, Harayama T, Yanagida K, and Shimizu T. Lysophosphatidylcholine acyltransferase 3 is the key enzyme for incorporating arachidonic acid into glycerophospholipids during adipocyte differentiation. *Int J Mol Sci.* 2012;13(12):16267-80.
28. Martin SA, Gijon MA, Voelker DR, and Murphy RC. Measurement of lysophospholipid acyltransferase activities using substrate competition. *J Lipid Res.* 2014;55(4):782-91.
29. Li S, Song KS, and Lisanti MP. Expression and characterization of recombinant caveolin. Purification by polyhistidine tagging and cholesterol-dependent incorporation into defined lipid membranes. *J Biol Chem.* 1996;271(1):568-73.
30. Murata M, Peranen J, Schreiner R, Wieland F, Kurzchalia TV, and Simons K. VIP21/caveolin is a cholesterol-binding protein. *Proc Natl Acad Sci U S A.* 1995;92(22):10339-43.
31. Janes PW, Ley SC, and Magee AI. Aggregation of lipid rafts accompanies signaling via the T cell antigen receptor. *J Cell Biol.* 1999;147(2):447-61.
32. Chambers K, and Brown WJ. Characterization of a novel CI-976-sensitive lysophospholipid acyltransferase that is associated with the Golgi complex. *Biochem Biophys Res Commun.* 2004;313(3):681-6.
33. Chambers K, Judson B, and Brown WJ. A unique lysophospholipid acyltransferase (LPAT) antagonist, CI-976, affects secretory and endocytic membrane trafficking pathways. *J Cell Sci.* 2005;118(Pt 14):3061-71.
34. McCarthy JJ, Srikuea R, Kirby TJ, Peterson CA, and Esser KA. Inducible Cre transgenic mouse strain for skeletal muscle-specific gene targeting. *Skelet Muscle.* 2012;2(1):8.

35. Hishikawa D, Shindou H, Kobayashi S, Nakanishi H, Taguchi R, and Shimizu T. Discovery of a lysophospholipid acyltransferase family essential for membrane asymmetry and diversity. *Proc Natl Acad Sci U S A.* 2008;105(8):2830-5.
36. Gijon MA, Riekhof WR, Zarini S, Murphy RC, and Voelker DR. Lysophospholipid acyltransferases and arachidonate recycling in human neutrophils. *J Biol Chem.* 2008;283(44):30235-45.
37. Vainio S, Heino S, Mansson JE, Fredman P, Kuismanen E, Vaarala O, and Ikonen E. Dynamic association of human insulin receptor with lipid rafts in cells lacking caveolae. *EMBO Rep.* 2002;3(1):95-100.
38. Foti M, Porcheron G, Fournier M, Maeder C, and Carpentier JL. The neck of caveolae is a distinct plasma membrane subdomain that concentrates insulin receptors in 3T3-L1 adipocytes. *Proc Natl Acad Sci U S A.* 2007;104(4):1242-7.
39. Kabayama K, Sato T, Saito K, Loberto N, Prinetti A, Sonnino S, Kinjo M, Igarashi Y, and Inokuchi J. Dissociation of the insulin receptor and caveolin-1 complex by ganglioside GM3 in the state of insulin resistance. *Proc Natl Acad Sci U S A.* 2007;104(34):13678-83.
40. Hahn-Obercyger M, Graeve L, and Madar Z. A high-cholesterol diet increases the association between caveolae and insulin receptors in rat liver. *J Lipid Res.* 2009;50(1):98-107.
41. Capozza F, Combs TP, Cohen AW, Cho YR, Park SY, Schubert W, Williams TM, Brasaemle DL, Jelicks LA, Scherer PE, et al. Caveolin-3 knockout mice show increased adiposity and whole body insulin resistance, with ligand-induced insulin receptor instability in skeletal muscle. *Am J Physiol Cell Physiol.* 2005;288(6):C1317-31.
42. Oshikawa J, Otsu K, Toya Y, Tsunematsu T, Hankins R, Kawabe J, Minamisawa S, Umemura S, Hagiwara Y, and Ishikawa Y. Insulin resistance in skeletal muscles of caveolin-3-null mice. *Proc Natl Acad Sci U S A.* 2004;101(34):12670-5.
43. Deng YF, Huang YY, Lu WS, Huang YH, Xian J, Wei HQ, and Huang Q. The Caveolin-3 P104L mutation of LGMD-1C leads to disordered glucose metabolism in muscle cells. *Biochem Biophys Res Commun.* 2017;486(2):218-23.
44. Shang L, Chen T, Xian J, Deng Y, Huang Y, Zhao Q, Liang G, Liang Z, Lian F, Wei H, et al. The caveolin-3 P104L mutation in LGMD-1C patients inhibits non-insulin-stimulated glucose metabolism and growth but promotes myocyte proliferation. *Cell Biol Int.* 2019;43(6):669-77.
45. Huang Y, Deng Y, Shang L, Yang L, Huang J, Ma J, Liao X, Zhou H, Xian J, Liang G, et al. Effect of type 2 diabetes mellitus caveolin-3 K15N mutation on glycometabolism. *Exp Ther Med.* 2019;18(4):2531-9.
46. Shang L, Chen T, Deng Y, Huang Y, Huang Y, Xian J, Lu W, Yang L, and Huang Q. Caveolin-3 promotes glycometabolism, growth and proliferation in muscle cells. *PLoS One.* 2017;12(12):e0189004.
47. Simons K, and Toomre D. Lipid rafts and signal transduction. *Nat Rev Mol Cell Biol.* 2000;1(1):31-9.
48. Galbiati F, Engelman JA, Volonte D, Zhang XL, Minetti C, Li M, Hou H, Jr., Kneitz B, Edelmann W, and Lisanti MP. Caveolin-3 null mice show a loss of caveolae, changes in the microdomain distribution of the dystrophin-glycoprotein complex, and t-tubule abnormalities. *J Biol Chem.* 2001;276(24):21425-33.
49. Uhles S, Moede T, Leibiger B, Berggren PO, and Leibiger IB. Isoform-specific insulin receptor signaling involves different plasma membrane domains. *J Cell Biol.* 2003;163(6):1327-37.
50. Shulman GI. Cellular mechanisms of insulin resistance. *The Journal of clinical investigation.* 2000;106(2):171-6.

51. Chavez JA, and Summers SA. A ceramide-centric view of insulin resistance. *Cell Metab.* 2012;15(5):585-94.
52. Kien CL, Bunn JY, Poynter ME, Stevens R, Bain J, Ikayeva O, Fukagawa NK, Champagne CM, Crain KI, Koves TR, et al. A lipidomics analysis of the relationship between dietary fatty acid composition and insulin sensitivity in young adults. *Diabetes.* 2013;62(4):1054-63.
53. Timmers S, Nabben M, Bosma M, van Bree B, Lenaers E, van Beurden D, Schaart G, Westerterp-Plantenga MS, Langhans W, Hesselink MK, et al. Augmenting muscle diacylglycerol and triacylglycerol content by blocking fatty acid oxidation does not impede insulin sensitivity. *Proc Natl Acad Sci U S A.* 2012;109(29):11711-6.
54. Demeure O, Lecerf F, Duby C, Desert C, Ducheix S, Guillou H, and Lagarrigue S. Regulation of LPCAT3 by LXR. *Gene.* 2011;470(1-2):7-11.
55. Yamazaki T, Hirose A, Sakamoto T, Okazaki M, Mitsumoto A, Kudo N, and Kawashima Y. Peroxisome proliferators attenuate free arachidonic acid pool in the kidney through inducing lysophospholipid acyltransferases. *J Pharmacol Sci.* 2009;111(2):201-10.
56. Heden TD, Ryan TE, Ferrara PJ, Hickner RC, Brophy PM, Neufer PD, McClung JM, and Funai K. Greater Oxidative Capacity in Primary Myotubes from Endurance-trained Women. *Med Sci Sports Exerc.* 2017;49(11):2151-7.
57. Heden TD, Johnson JM, Ferrara PJ, Eshima H, Verkerke ARP, Wentzler EJ, Siripoksup P, Narowski TM, Coleman CB, Lin CT, et al. Mitochondrial PE potentiates respiratory enzymes to amplify skeletal muscle aerobic capacity. *Science advances.* 2019;5(9):eaax8352.
58. Verkerke ARP, Ferrara PJ, Lin C-T, Johnson JM, Ryan TE, Maschek JA, Eshima H, Paran CW, Laing BT, Siripoksup P, et al. Phospholipid methylation regulates muscle metabolic rate through Ca2+ transport efficiency. *Nature Metabolism.* 2019;1(9):876-85.
59. Johnson JM, Verkerke ARP, Maschek JA, Ferrara PJ, Lin C-T, Kew KA, Neufer PD, Lodhi IJ, Cox JE, and Funai K. Alternative splicing of UCP1 by non-cell-autonomous action of PEMT. *Molecular Metabolism.* 2020;31(55-66.
60. Zeczycki TN, Whelan J, Hayden WT, Brown DA, and Shaikh SR. Increasing levels of cardiolipin differentially influence packing of phospholipids found in the mitochondrial inner membrane. *Biochem Biophys Res Commun.* 2014;450(1):366-71.
61. Park S, Turner KD, Zheng D, Brault JJ, Zou K, Chaves AB, Nielsen TS, Tanner CJ, Treebak JT, and Houmard JA. Electrical pulse stimulation induces differential responses in insulin action in myotubes from severely obese individuals. *J Physiol.* 2019;597(2):449-66.
62. Al-Khalili L, Chibalin AV, Kannisto K, Zhang BB, Permert J, Holman GD, Ehrenborg E, Ding VD, Zierath JR, and Krook A. Insulin action in cultured human skeletal muscle cells during differentiation: assessment of cell surface GLUT4 and GLUT1 content. *Cell Mol Life Sci.* 2003;60(5):991-8.
63. Funai K, Lodhi IJ, Spears LD, Yin L, Song H, Klein S, and Semenkovich CF. Skeletal Muscle Phospholipid Metabolism Regulates Insulin Sensitivity and Contractile Function. *Diabetes.* 2016;65(2):358-70.
64. Funai K, Song H, Yin L, Lodhi IJ, Wei X, Yoshino J, Coleman T, and Semenkovich CF. Muscle lipogenesis balances insulin sensitivity and strength through calcium signaling. *The Journal of clinical investigation.* 2013;123(3):1229-40.
65. Ferrara PJ, Verkerke ARP, Brault JJ, and Funai K. Hypothermia Decreases O2 Cost for Ex Vivo Contraction in Mouse Skeletal Muscle. *Med Sci Sports Exerc.* 2018;50(10):2015-23.
66. Mendez JaK, A. . Density and Composition of Mammalian Muscle. *Metabolism.* 1960;9(4.

67. Moorwood C, Liu M, Tian Z, and Barton ER. Isometric and eccentric force generation assessment of skeletal muscles isolated from murine models of muscular dystrophies. *J Vis Exp.* 201371):e50036.
68. Brooks SV, and Faulkner JA. Contractile properties of skeletal muscles from young, adult and aged mice. *J Physiol.* 1988;404(71-82.
69. Rockett BD, Teague H, Harris M, Melton M, Williams J, Wassall SR, and Shaikh SR. Fish oil increases raft size and membrane order of B cells accompanied by differential effects on function. *J Lipid Res.* 2012;53(4):674-85.
70. Otsu N. Threshold Selection Method from Gray-Level Histograms. *Ieee T Syst Man Cyb.* 1979;9(1):62-6.
71. Sezgin M, and Sankur B. Survey over image thresholding techniques and quantitative performance evaluation. *J Electron Imaging.* 2004;13(1):146-68.
72. Shaikh SR, Rockett BD, Salameh M, and Carraway K. Docosahexaenoic acid modifies the clustering and size of lipid rafts and the lateral organization and surface expression of MHC class I of EL4 cells. *J Nutr.* 2009;139(9):1632-9.

Figure 1

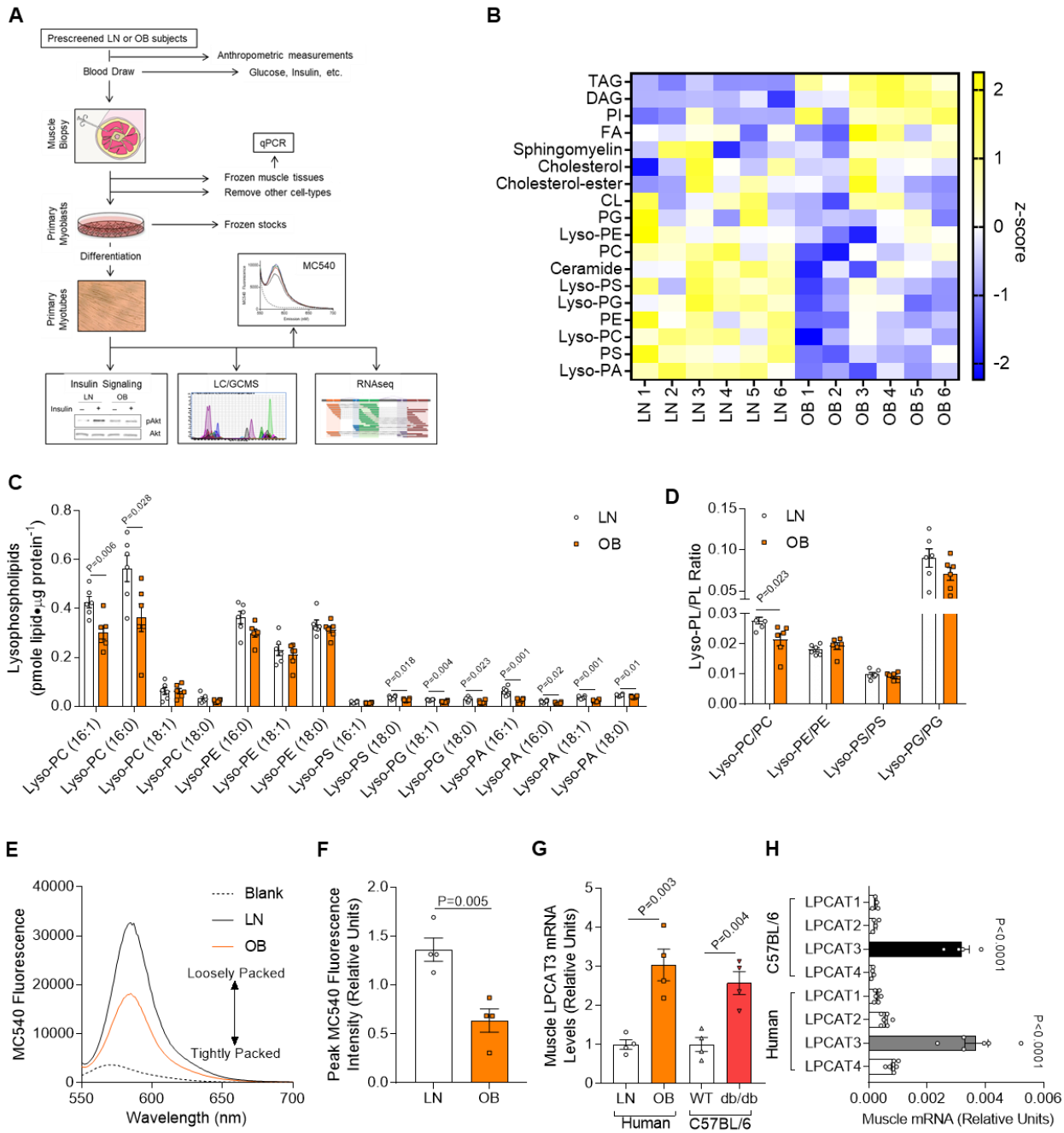

711

712 **Figure 1: Lipidomic analyses of skeletal muscle samples from lean and obese human**

713 **subjects.** (A) A schematic of the workflow for the clinical study. (B-D) Lipidomic analysis of

714 HSkMC from lean insulin-sensitive (LN) and obese insulin-resistant (OB) subjects. (B) Heat map

715 of lipid content by class. (C) Species of lysophospholipids. (D) Lysophospholipid to phospholipid

716 ratio (*n*=6). (E&F) Quantification of MC540 fluorescence in LN and OB HSkMC (*n*=4). (G)
717 LPCAT3 mRNA in muscle biopsies from LN or OB subjects (left), and in skeletal muscle of wild
718 type (WT) or a db/db (right) mice (*n*=4). (H) Expression of all isoforms of LPCAT in muscle
719 samples from mouse (*n*=4) or human (*n*=6) skeletal muscle. (C,D,F&G) Two-tailed t-tests. (H)
720 One-way ANOVA followed by post-hoc multiple comparisons. All data are represented as mean
721 ± SEM.
722

Figure 2

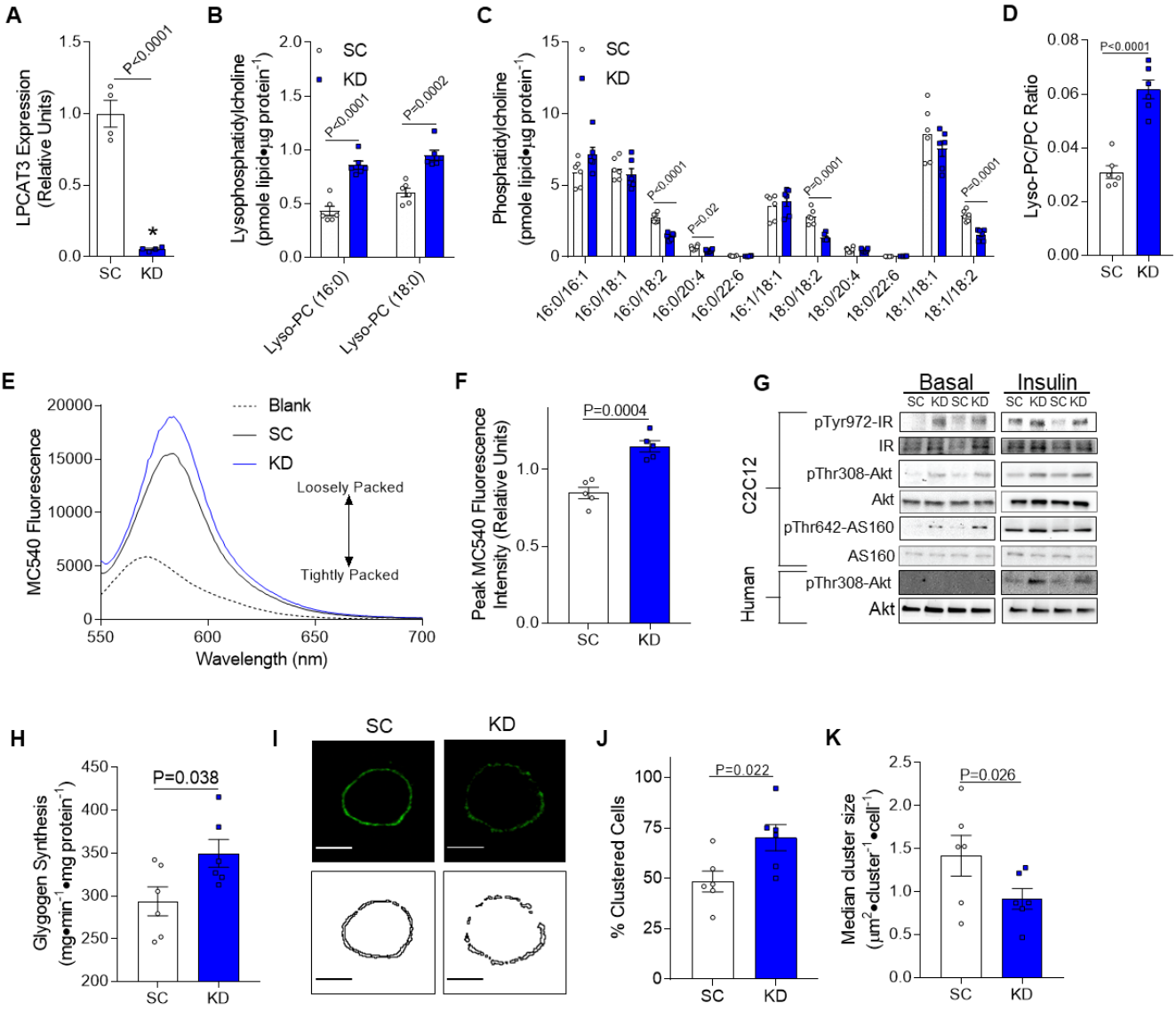

Figure 2: LPCAT3 knockdown enhances skeletal muscle insulin sensitivity *in vitro*. (A) LPCAT3 mRNA levels in myoblasts infected with lentiviruses expressing shRNA for scrambled (SC) or LPCAT3 sequences (KD) and differentiated into myotubes (*n*=4). (B-D) Lipids were extracted from C2C12 myotubes for analysis between SC and KD cells. Quantification of (B) lysophosphatidylcholine (lyso-PC), (C) phosphatidylcholine (PC), and (D) total lyso-PC/PC (*n*=6). (E&F) Quantification of MC540 fluorescence in SC and KD myotubes (*n*=5). (G)

Phosphorylation and total protein of IR, Akt, and AS160 were measured via Western blot with (0.6 nM) or without insulin in C2C12 myotubes (top) and human primary skeletal muscle cells (bottom). (H) Glycogen synthesis was quantified in C2C12 cells incubated with insulin (12 nM) (*n*=6). (I-K) GM-1 enriched microdomains were labeled in SC and KD round-up myotubes. (I) Plasma membrane GM-1 localization was visualized (top panels: fluorescence images, bottom panels: binary images). (J) Cells were scored as clustered or non-clustered between SC and KD myotubes. (K) Particle size was measured for each cell in 6 separate experiments and the median for each experiment was used as a representative of that experiment (n=35-50/experiment, 6 separate experiments). (A-D,F,H,J&K) Two-tailed t-tests were performed. All data are represented as mean ± SEM.

Figure 3

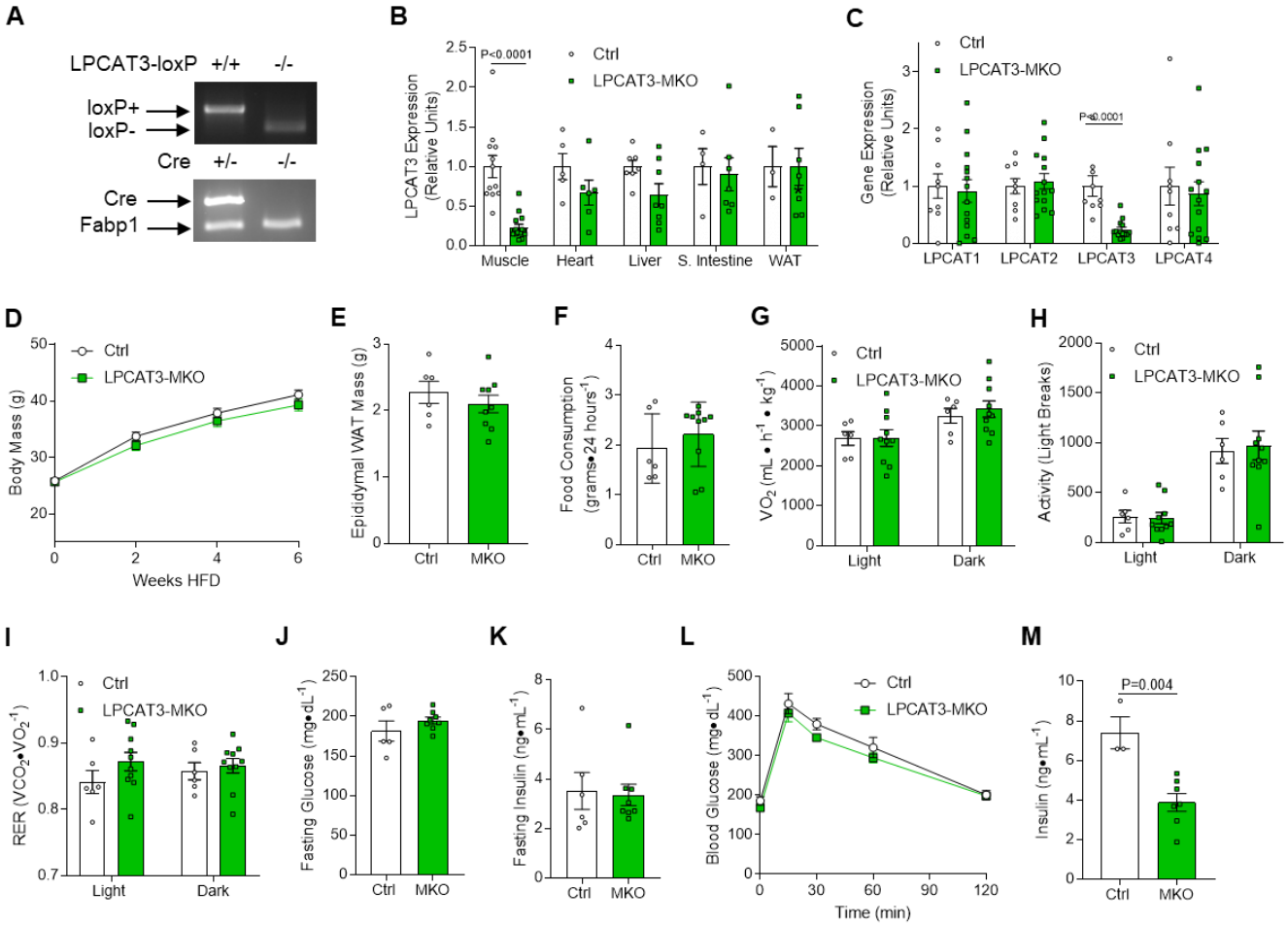

740

741 **Figure 3: Whole-body phenotyping of LPCAT3-MKO mice.** (A) Mice with tamoxifen-inducible
742 skeletal muscle-specific Cre-recombinase (HSA-MerCreMer+/-) were crossed with mice with
743 *LoxP* sites flanking exon3 of the *Lpcat3* gene (LPCAT3cKO+/+) to generate skeletal muscle-
744 specific inducible knock out of LPCAT3 (LPCAT3cKO+/+, HSA-MerCreMer+/-) (LPCAT3-MKO).
745 Littermates (LPCAT3cKO+/+, HSA-MerCreMer-/-) (Ctrl) were used as control mice for all
746 experiments. (B) LPCAT3 mRNA in tibialis anterior (TA, Muscle), heart, liver, small intestine (S.
747 Intestine), and inguinal white adipose tissue (WAT) (muscle: Ctrl *n*=12, MKO *n*=15; heart: Ctrl
748 *n*=5, MKO *n*=6; liver: Ctrl *n*=7, MKO *n*=8; S. Intestine: Ctrl *n*=4, MKO *n*=7; WAT: Ctrl *n*=3, MKO
749 *n*=7). (C) mRNA of all LPCAT isoforms in TA muscles of Ctrl and LPCAT3-MKO mice (Ctrl *n*=9,

MKO *n*=14) (D) Body mass during high-fat diet (HFD) feeding in Ctrl and LPCAT3-MKO mice (Ctrl *n*=8, MKO *n*=11). (E) Epididymal WAT mass (Ctrl *n*=6, MKO *n*=9). (F-I) Ctrl and LPCAT3-MKO mice were placed in metabolic chambers for measurement of (F) food consumption, (G) VO_2, (H) activity, and (I) respiratory exchange ratio (RER) (Ctrl *n*=6, MKO *n*=10). (J) Fasting glucose (Ctrl *n*=5, MKO *n*=9). (K) Fasting insulin (Ctrl *n*=6, MKO *n*=9). (L) Intraperitoneal glucose tolerance test (Ctrl *n*=6, MKO *n*=8). (M) Serum insulin at the 30-minute time point of the glucose tolerance test (Ctrl *n*=3, MKO *n*=8). All data except (A) are from HFD-fed mice. (B,C,E-K&M) Two-tailed t-tests or (D&L) 2-way ANOVA with Sidak's multiple comparisons test were performed. All data are represented as mean ± SEM.

Figure 4

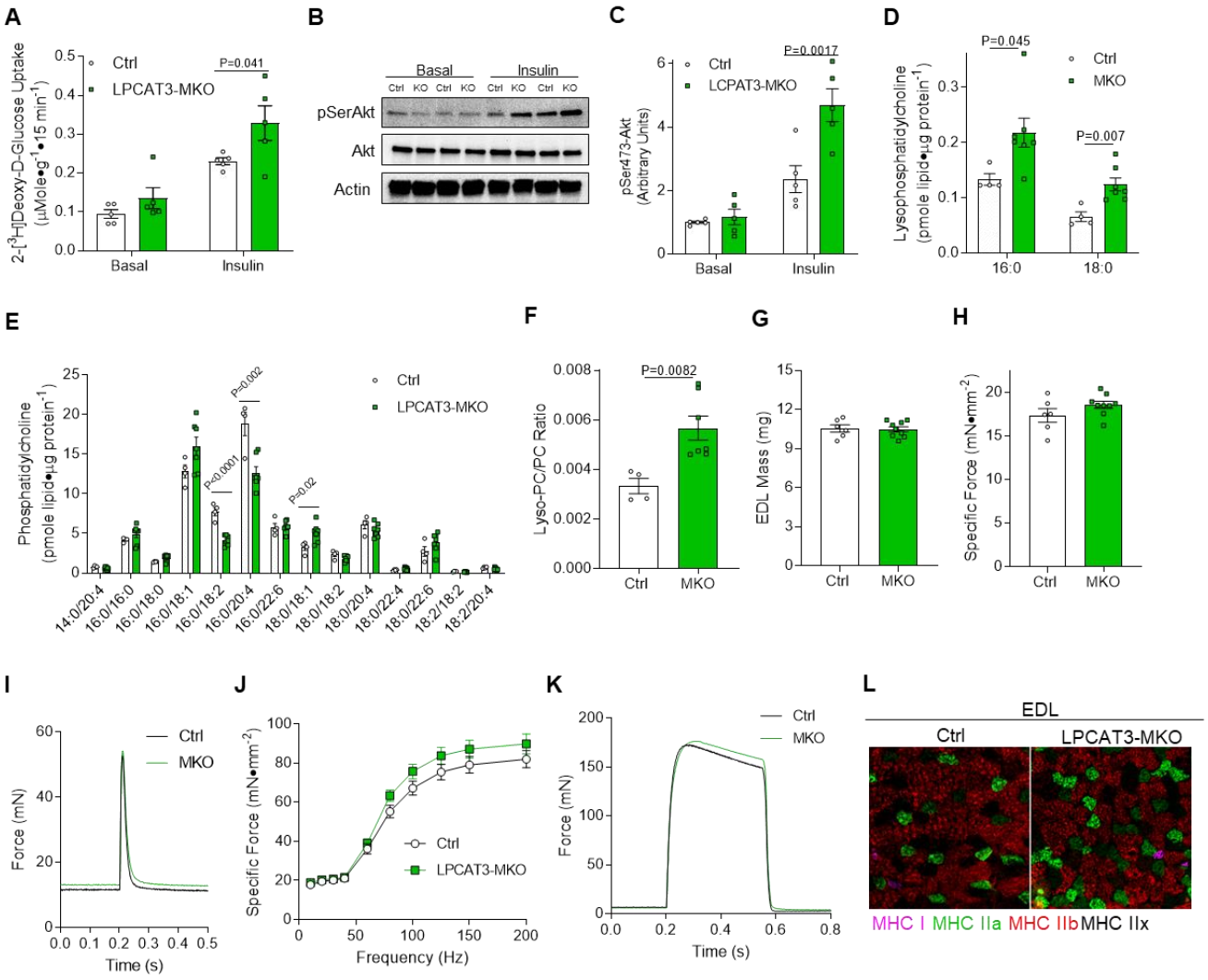

760

761 **Figure 4: LPCAT3-MKO mice are protected from diet-induced skeletal muscle insulin**

762 **resistance.** (A-C) Soleus muscles were dissected and incubated with or without 200 µU/mL of

763 insulin. (A) *Ex vivo* 2-deoxyglucose uptake (*n*=5). (B&C) Ser473 phosphorylation and total Akt

764 (Ctrl *n*=5, MKO *n*=6). (D-F) Lipids were extracted from gastrocnemius muscles of Ctrl and

765 LPCAT3-MKO mice for mass spectrometric analysis. Quantification of (D) lyso-PC, (E) PC, and

766 (F) total lyso-PC/PC (Ctrl *n*=4, MKO *n*=7). (G-L) Extensor digitorum longus (EDL) muscles of

767 Ctrl and LPCAT3-MKO mice were dissected for measurement of (G) mass, (H&I) force

768 produced with a pulse stimulation, (J&K) force produced with tetanic stimulation ranging from

769 10-200 Hz (K, force tracing at 200 Hz stimulation) (Ctrl *n*=6, MKO *n*=9), and (L) skeletal muscle
770 fiber-type (MHC I: pink, MHC IIa: green, MHC IIb:red, and MHC IIx: negative). All data are from
771 HFD-fed mice. (A,C&J) 2-way ANOVA with Sidak's multiple comparisons test or (D-H) two-tailed
772 t-tests were performed. All data are represented as mean ± SEM.

Figure 5

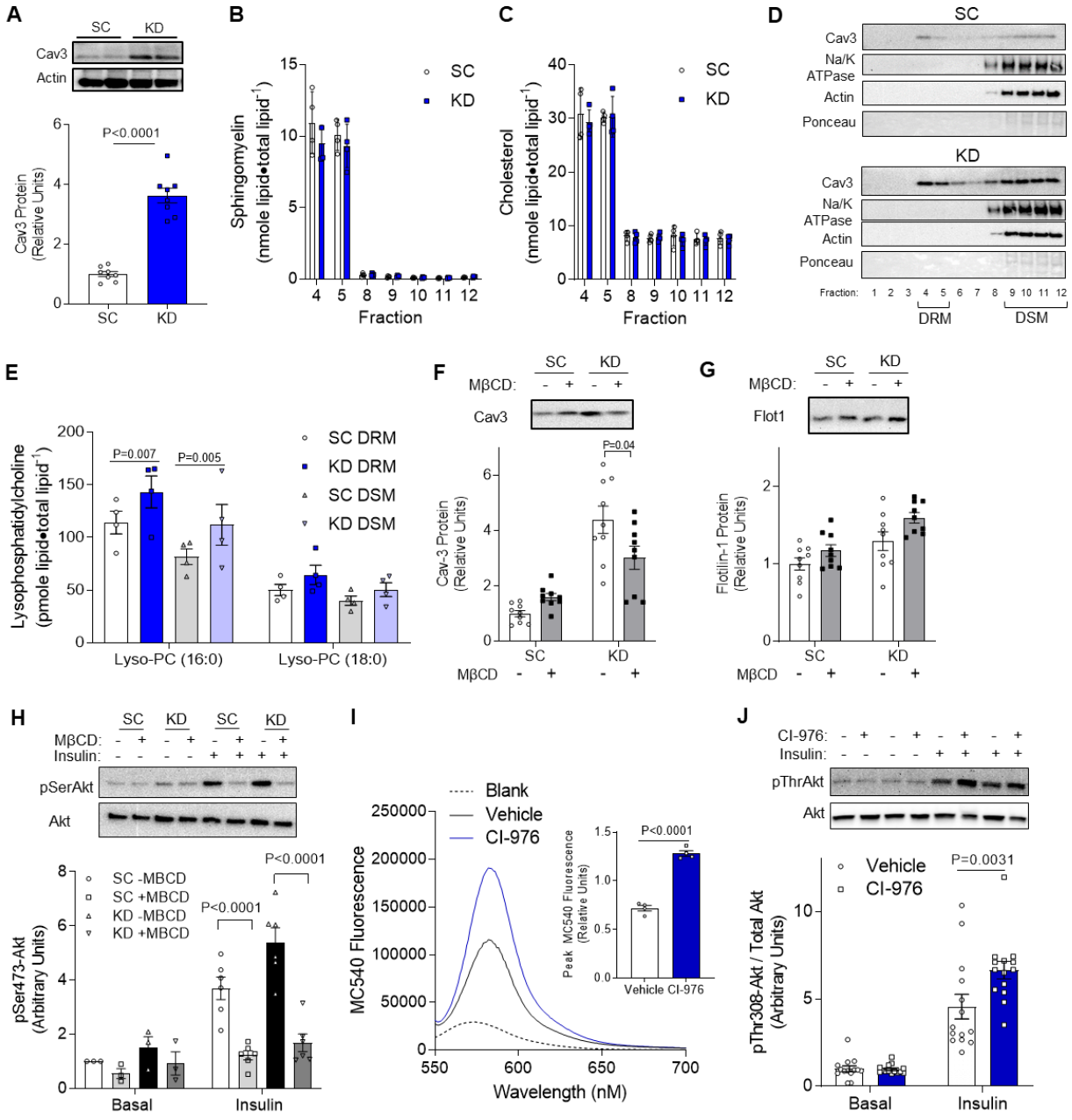

Figure 5: LPCAT3 deletion alters plasma membrane organization. C2C12 cells were infected with lentiviruses expressing shRNA for scrambled (SC) or LPCAT3 (KD) and differentiated into myotubes. (A) Caveolin-3 (cav3) protein content. (B&C) Detergent-resistant membranes (DRM; fractions 4&5) and detergent-soluble membranes (DSM; fractions 8-12)

778 were isolated and lipids were extracted for quantification of (B) sphingomyelin and (C)
779 cholesterol (*n*=4). (D) Cav3, Na/K ATPase, actin, and total protein content were assessed via
780 Western blot in all fractions from the sucrose gradient. (E) Lyso-PC levels in DSM and DRM
781 isolations (*n*=4). (F-H) C2C12 myotubes were incubated in the presence (10 mM) or absence of
782 methyl-beta-cyclodextrin (MβCD) for 1 hour. (F&G) MβCD successfully depletes cav3 ($P<0.001$,
783 main effect of LPCAT3 knockdown) but not flotillin1 ($P=0.003$ main effect of LCPAT3
784 knockdown, $P=0.01$ main effect of MβCD) (n=9). (H) Cells were incubated in the presence (0.6
785 nM) or absence of insulin and were blotted for total or Ser473 phosphorylation of Akt (n=3
786 Basal, n=6 Insulin). (I&J) C2C12 myoblasts were differentiated into myotubes with either CI-976
787 or vehicle. (I) Quantification of MC540 fluorescence (*n*=6). (J) Western blot of Thr308
788 phosphorylation and total Akt in the presence (12 nM) and absence of insulin (*n*=14, $P=0.024$
789 main effect of insulin) (A-C&I) Two-tailed t-tests or (E-H&J) 2-way ANOVA with Sidak's multiple
790 comparisons test were performed. All data are represented as mean ± SEM.
791

Figure 6

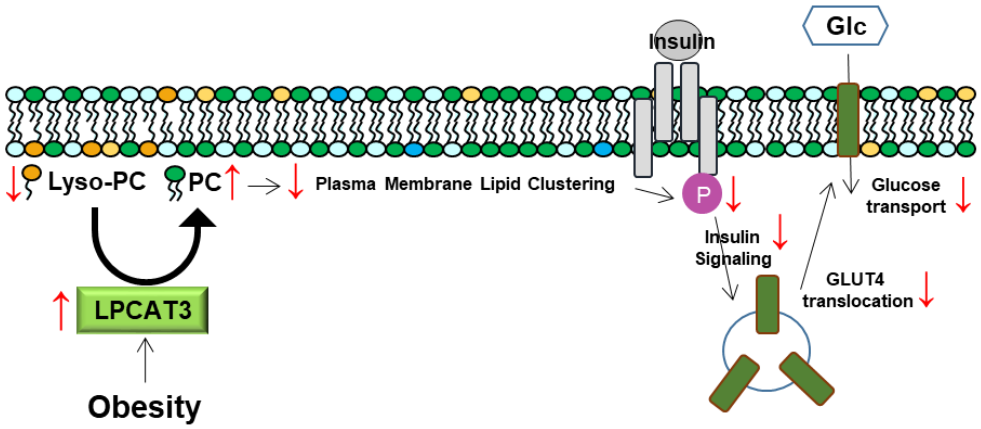

792

793 **Figure 6: A proposed mechanism of action by which LPCAT3 promotes diet-induced**

794 **skeletal muscle insulin resistance.**

795

Figure S1

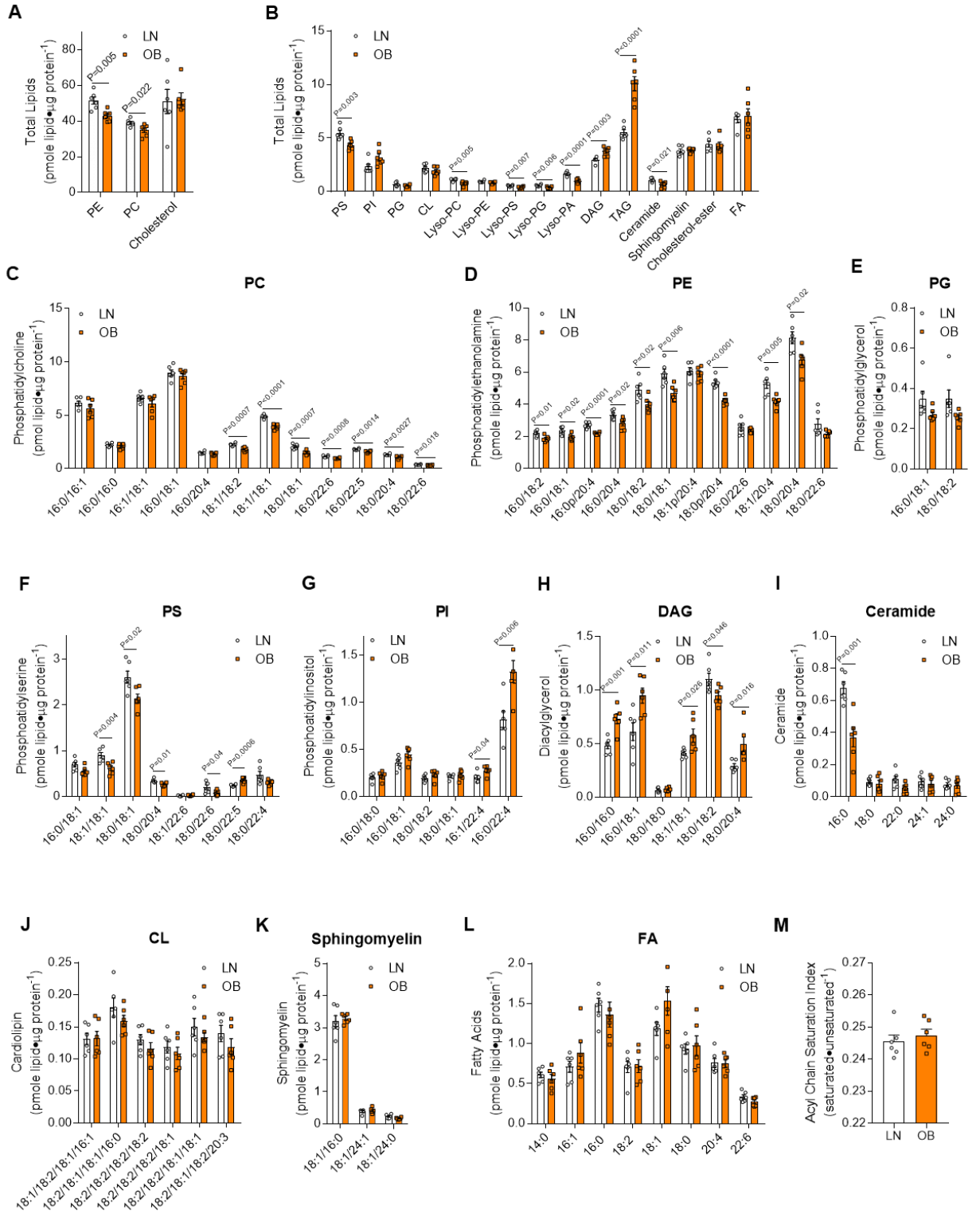

796

Figure S1: Lipid quantification in LN and OB HSkMC. (A-M) Muscle biopsies were taken from LN or OB human subjects and primary skeletal muscle cells were isolated and differentiated. Quantification of (A&B) total lipids by class, and species of (C) phosphatidylcholine (PC), (D) phosphatidylethanolamine (PE), (E) phosphatidylglycerol (PG), (F) phosphatidylserine (PS), (G) phosphatidylinositol (PI), (H) diacylglycerol (DAG), (I) ceramide, (J) cardiolipin (CL), (K) sphingomyelin, and (L) fatty acid (FA). (M) Quantification of the acyl chain saturation index of all detectable phospholipids. (*n*=6). Two-tailed t-tests were performed for all analyses. All data are represented as mean ± SEM.

Figure S2

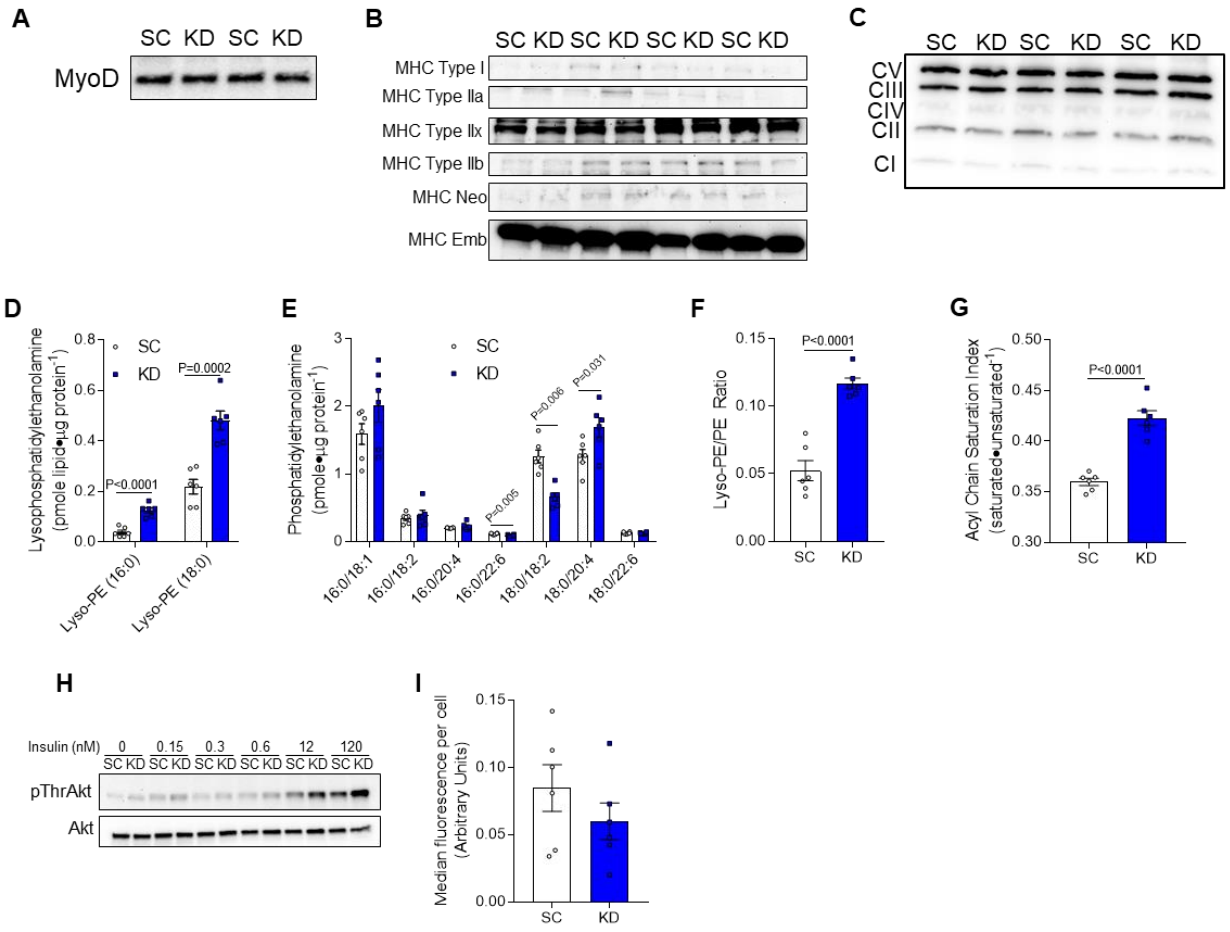

Figure S2: Knockdown of LPCAT3 in C2C12 myotubes. C2C12 myoblasts were infected with shRNA generating lentiviruses targeting scrambled (shScrambled; SC) or LPCAT3 (shLPCAT3; KD) to decrease LPCAT3 expression and cells were differentiated into myotubes. (A-C) Western blot in SC and KD cells probing for (A) MyoD, (B) myosin heavy chain isoforms, and (C) complexes I-V of the electron transport chain. (D-G) Lipids were extracted in SC and KD myotubes for quantification of (D) lyso-PE, (E) PE species, (F) total lyso-PE/PE, and (G) acyl chain saturation index of phospholipids (*n*=6). (H) Thr308 phosphorylation and total Akt from cells incubated (10 min) with various concentrations of insulin. (I) GM-1 microdomains were labeled with GFP and cross-linked to induce patching in SC and KD C2C12 myotubes. Total fluorescence in each cell was measured across 6 separate experiments (*n*=35-50/experiment)

817 and the median of each experiment was used as a representative. Two-tailed t-tests were

818 performed. All data are represented as mean ± SEM.

Figure S3

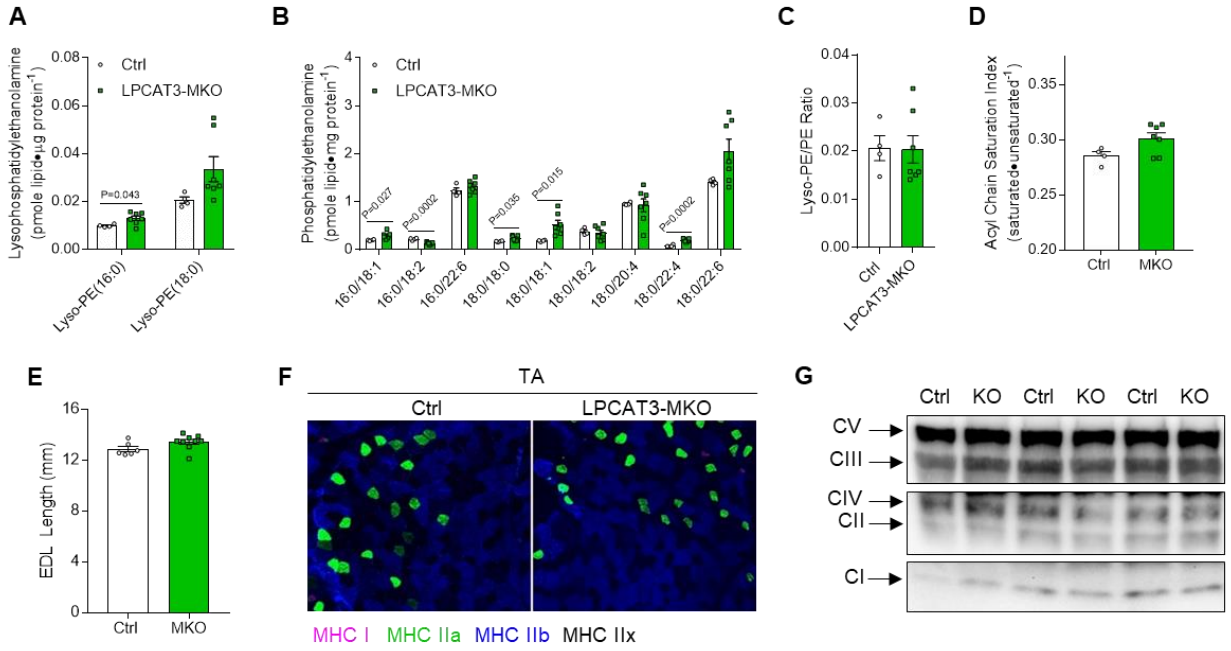

Figure S3: Additional data on muscles from HFD-fed Ctrl and LPCAT3-MKO mice. (A-D) Lipids were extracted from gastrocnemius muscles of Ctrl and LPCAT3-MKO mice for analysis. Quantification of (A) lyso-PE species, (B) PE species, (C) total lyso-PE/PE, and (D) phospholipid acyl chain saturation index (Ctrl *n*=4, MKO *n*=7). (E) Muscle lengths of extensor digitorum longus (EDL) muscles (Ctrl *n*=6, MKO *n*=9). (F) Skeletal muscle fiber-type (MHC I: pink, MHC IIa: green, MHC IIb:blue, and MHC IIx: negative) of tibialis anterior (TA) muscles**.** (G) Measurement of complexes I-V of the electron transport chain in TA muscles from Ctrl and LPCAT3-MKO mice. (A-E) Two-tailed t-tests. All data are represented as mean ± SEM.

Figure S4

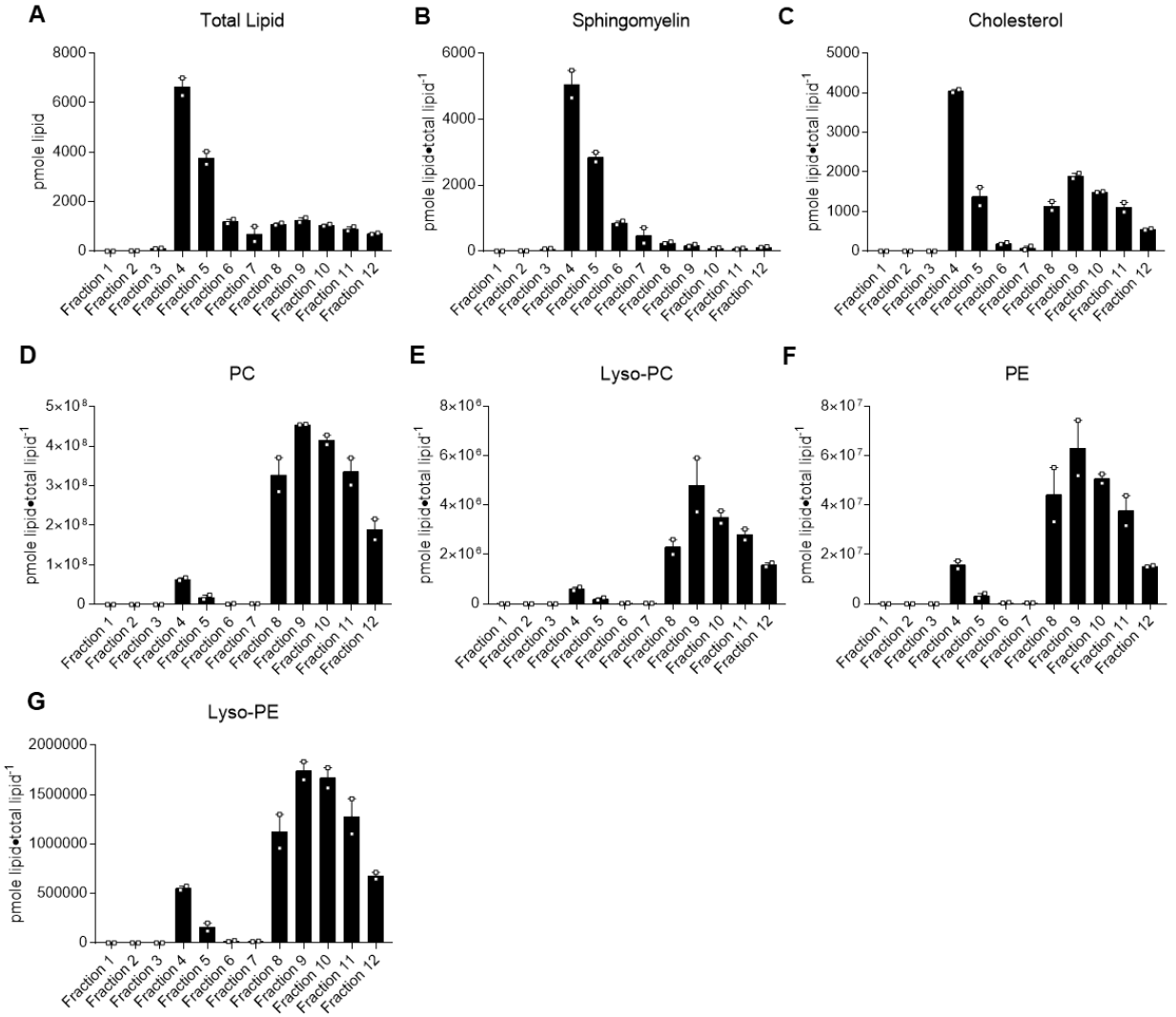

828

829 **Figure S4: Lipid contents of detergent-resistant and detergent-soluble membrane**

830 **fractions.** (A-G) Wild type C2C12 myotubes were suspended in a sucrose gradient and purified

831 via ultracentrifugation to separate detergent-resistant membrane (DRM) fractions from detergent

832 soluble membrane (DSM) fractions. After ultracentrifugation fractions were analyzed for (A) total

833 lipid content, (B) sphingomyelin, (C) cholesterol, (D) PC, (E) lyso-PC, (F) PE, and (G) lyso-PE

834 (*n*=2). All data are represented as mean ± SEM.

Figure S5

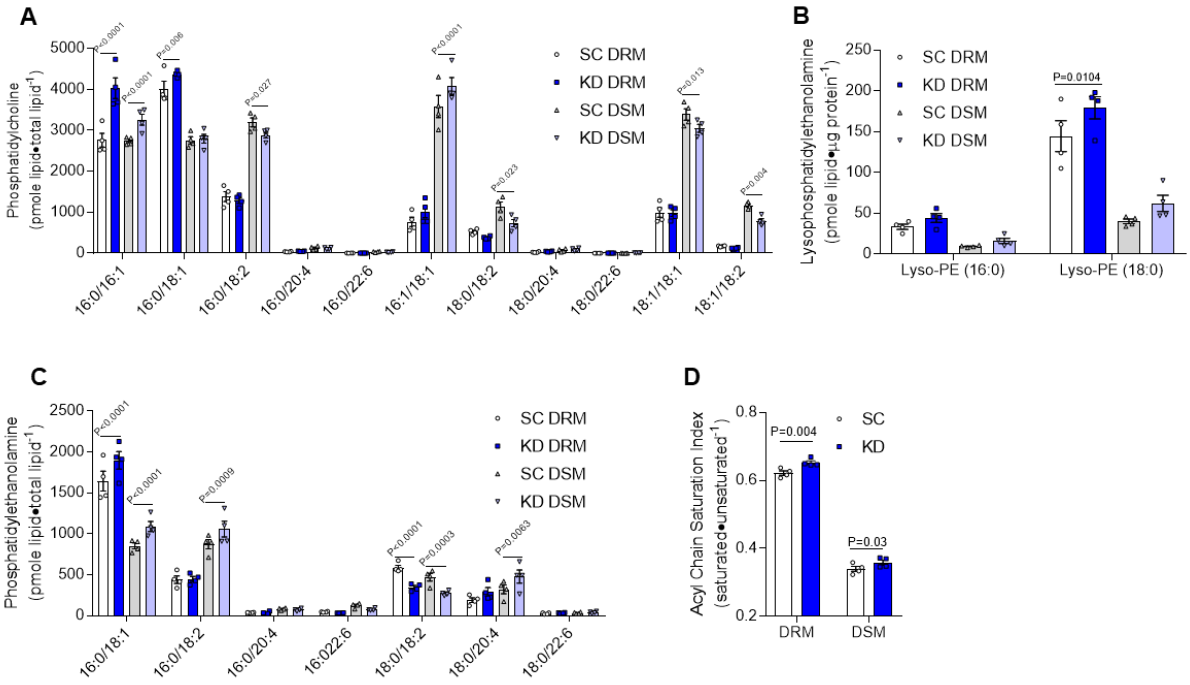

Figure S5: Plasma membrane microdomains and phospholipid composition in membrane fractions with LPCAT3 inhibition. (A-D) SC and KD C2C12 myotubes were suspended in a sucrose density gradient and purified with ultracentrifugation. (A) PC, (B) lyso-PE, (C) PE species, and (D) acyl chain saturation index of all phospholipids were quantified in DRM and DSM fractions (*n*=4). (D) Two-tailed t-tests or (A-C) 2-way ANOVA with Sidak's multiple comparisons test were performed. All data are represented as mean ± SEM.

842 **Table S1:** Subject characteristics of lean insulin-sensitive (LN) and obese insulin-resistant (OB)
843 subjects (*n*=6/group).

	LN	OB	p
Age (year)	30.2±3.5	35.8±3.1	0.25
Height (cm)	162.4±2.8	166.9±2.6	0.26
Weight (kg)	62.9±2.4	126.1±8.0	<0.0001
BMI ($kg \cdot m^{-2}$)	23.85±0.67	45.0±1.85	<0.0001
Glucose ($mg \cdot dL^{-1}$)	81.3±1.0	92.3±4.3	0.031
Insulin ($\mu U \cdot mL^{-1}$)	6.4±1.3	15.9±1.3	0.0004
HOMA-IR	1.29±0.27	3.6±0.44	0.001
Cholesterol ($mg \cdot dL^{-1}$)	177.7±13.0	177±12.9	0.97
HDL ($mg \cdot dL^{-1}$)	55.2±2.3	47.0±2.9	0.050
LDL ($mg \cdot dL^{-1}$)	105.2±11.9	109.5±8.6	0.78
Triglycerides ($mg \cdot dL^{-1}$)	86.8±19.8	102.7±23.7	0.62

844

845

846 **Table S2:** Primers used for quantitative-RT-PCR.

Gene	Species	F/R	Sequence (5'→3')
L32	Mouse	F	TTCCTGGTCCACAATGTCAA
		R	GGCTTTTCGGTTCTTAGAGGA
LPCAT1	Mouse	F	CACGAGCTGCGACTGAGC
		R	ATGAAAGCAGCGAACAGGAG
LPCAT2	Mouse	F	ACCTGTTTCCGATGTCCTGA
		R	CCAGGCCGATCACATACTCT
LPCAT3	Mouse	F	GGCCTCTCAATTGCTTATTTCA
		R	AGCACGACACATAGCAAGGA
LPCAT4	Mouse	F	GAGTTACACCTCTCCGGCCT
		R	GGCCAGAGGAGAAAGAGGAC
L32	Human	F	GTCAAGGAGCTGGAAGTGCT
		R	CTCTTTCCACGATGGCTTTG
LPCAT1	Human	F	CAGGCCAGCAGCATCAT
		R	TCAGCGCCCTGCAGAAG
LPCAT2	Human	F	TTGCCTGTTTCAGATGTCTTG
		R	GCCAGGCCAATCACATACTC
LPCAT3	Human	F	AGCCTTAACAAGTTGGCGAC
		R	TGCCGATAAAACAAAGCAAA
LPCAT4	Human	F	CCCTTCGTGCATGAGTTACA
		R	ATAAAGGCCAGAAGCACTCG
Caveolin3	Mouse	F	GGATCTGGAAGCTCGGATCAT
		R	TCCGCAATCACGTCTTCAAAAT

847